Cell Metabolism

Formation of I_2+III_2 supercomplex rescues respiratory chain defects

Graphical abstract

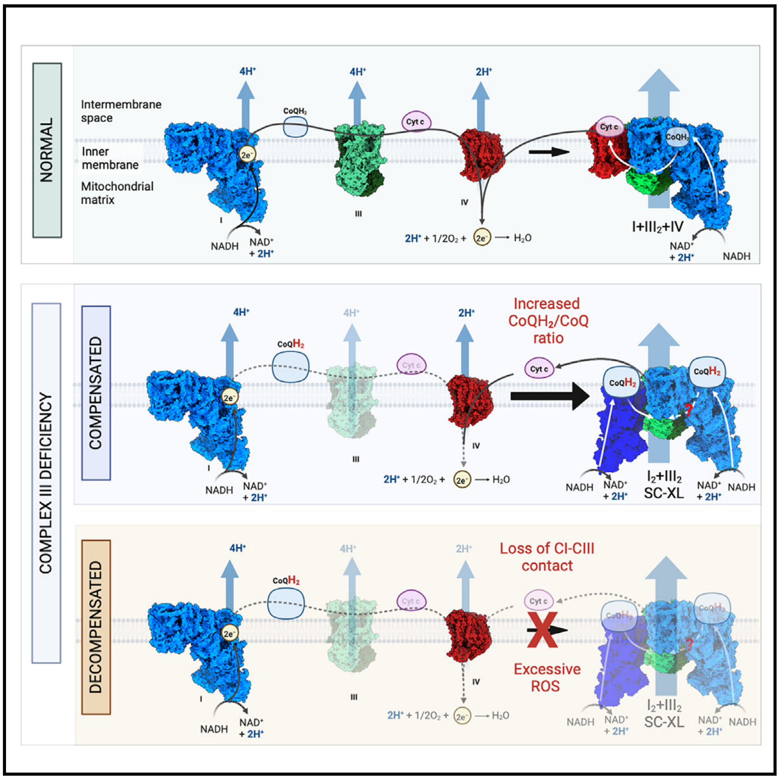

Highlights

- SC-XL (I_2+III_2) is a unique mammalian SC that mitigates CIII deficiency
- SC-XL formation is a mitohormetic response to coenzyme Q over-reduction
- SC-XL supports efficient OXPHOS with reduced CIII reactive oxygen species
- SC-XL is associated with protection against ischemic heart failure

Authors

Chao Liang, Abhilash Padavannil, Shan Zhang, ..., David A. Stroud, James A. Letts, Lena Ho

Correspondence

lena@ho-lab.org

In brief

Respiratory supercomplexes are conserved throughout evolution, but their physiological relevance remains contentious. Here, Liang et al. discover an I_2+III_2 supercomplex (SC-XL) triggered by complex III deficiency that rescues respiration by enhancing OXPHOS and reducing ROS production. These findings indicate that supercomplexes are indispensable for maintaining mitochondrial homeostasis and integrity during metabolic stress.

Liang et al., 2025, Cell Metabolism *37*, 1–19
February 4, 2025
https://doi.org/10.1016/j.cmet.2024.11.011

Please cite this article in press as: Liang et al., Formation of I_2+III_2 supercomplex rescues respiratory chain defects, Cell Metabolism (2024), https://doi.org/10.1016/j.cmet.2024.11.011

Cell Metabolism

CellPress

Article

Formation of I_2+III_2 supercomplex rescues respiratory chain defects

Chao Liang,[1,19] Abhilash Padavannil,[2,19] Shan Zhang,[1,18,19] Sheryl Beh,[1] David R.L. Robinson,[3] Jana Meisterknecht,[4] Alfredo Cabrera-Orefice,[4] Timothy R. Koves,[5] Chika Watanabe,[6] Miyuki Watanabe,[6] María Illescas,[7] Radiance Lim,[1] Jordan M. Johnson,[8] Shuxun Ren,[1] Ya-Jun Wu,[9] Dennis Kappei,[10,11,12] Anna Maria Ghelli,[13] Katsuhiko Funai,[8] Hitoshi Osaka,[6] Deborah Muoio,[5] Cristina Ugalde,[7,14,15] Ilka Wittig,[4] David A. Stroud,[3,16,17] James A. Letts,[2] and Lena Ho[1,20,*]

[1]Cardiovascular and Metabolic Diseases, Duke-NUS Medical School, Singapore, Singapore
[2]Department of Molecular and Cellular Biology, University of California, Davis, Davis, CA, USA
[3]Department of Biochemistry and Pharmacology, The Bio21 Molecular Science & Biotechnology Institute, University of Melbourne, Melbourne, VIC, Australia
[4]Functional Proteomics, Institute of Cardiovascular Physiology, Goethe University, Frankfurt am Main, Germany
[5]Duke Molecular Physiology Institute, Duke University, Durham, NC, USA
[6]Department of Pediatrics, Jichi Medical School, Shimotsuke-shi, Tochigi, Japan
[7]Instituto de Investigación Hospital 12 de Octubre, Madrid, Spain
[8]Diabetes and Metabolism Research Center, The University of Utah, Salt Lake City, UT, USA
[9]Department of Anatomy, Yong Loo Lin School of Medicine, National University of Singapore, Singapore, Singapore
[10]Cancer Science Institute of Singapore, National University of Singapore, Singapore, Singapore
[11]NUS Center for Cancer Research, Yong Loo Lin School of Medicine, National University of Singapore, Singapore, Singapore
[12]Department of Biochemistry, Yong Loo Lin School of Medicine, National University of Singapore, Singapore, Singapore
[13]Dipartimento di Farmacia e Biotecnologie (FABIT), Università di Bologna, 40126 Bologna, Italy
[14]Center for Biological Research Margarita Salas (CIB-CSIC), Madrid, Spain
[15]CIBER de Enfermedades Raras, U723, Madrid, Spain
[16]Murdoch Children's Research Institute, Royal Children's Hospital, Melbourne, VIC, Australia
[17]Victorian Clinical Genetics Services, Murdoch Children's Research Institute, Melbourne, VIC, Australia
[18]Present address: Department of Biochemistry, Department of Cardiology of First Affiliated Hospital, Zhejiang University School of Medicine, Hangzhou, China
[19]These authors contributed equally
[20]Lead contact
*Correspondence: lena@ho-lab.org

https://doi.org/10.1016/j.cmet.2024.11.011

SUMMARY

Mitochondrial electron transport chain (ETC) complexes partition between free complexes and quaternary assemblies known as supercomplexes (SCs). However, the physiological requirement for SCs and the mechanisms regulating their formation remain controversial. Here, we show that genetic perturbations in mammalian ETC complex III (CIII) biogenesis stimulate the formation of a specialized extra-large SC (SC-XL) with a structure of I_2+III_2, resolved at 3.7 Å by cryoelectron microscopy (cryo-EM). SC-XL formation increases mitochondrial cristae density, reduces CIII reactive oxygen species (ROS), and sustains normal respiration despite a 70% reduction in CIII activity, effectively rescuing CIII deficiency. Consequently, inhibiting SC-XL formation in CIII mutants using the Uqcrc1$^{DEL:E258-D260}$ contact site mutation leads to respiratory decompensation. Lastly, SC-XL formation promotes fatty acid oxidation (FAO) and protects against ischemic heart failure in mice. Our study uncovers an unexpected plasticity in the mammalian ETC, where structural adaptations mitigate intrinsic perturbations, and suggests that manipulating SC-XL formation is a potential therapeutic strategy for mitochondrial dysfunction.

INTRODUCTION

The electron transport chain (ETC) comprises four multi-protein complexes within the inner mitochondrial membrane (IMM): complex I (CI or NADH [nicotinamide adenine dinucleotide]:ubiquinone oxidoreductase), complex II (CII or succinate:ubiquinone oxidoreductase), complex III (CIII or ubiquinol-cytochrome *c* oxidoreductase), and complex IV (CIV or cytochrome *c* oxidase). These complexes transport electrons from donors to oxygen, generating a proton gradient that is used to drive ATP synthesis by complex V (ATP synthase). ETC complexes exist as free entities and supercomplexes (SCs). Depending on tissue

Please cite this article in press as: Liang et al., Formation of I_2+III_2 supercomplex rescues respiratory chain defects, Cell Metabolism (2024), https://doi.org/10.1016/j.cmet.2024.11.011

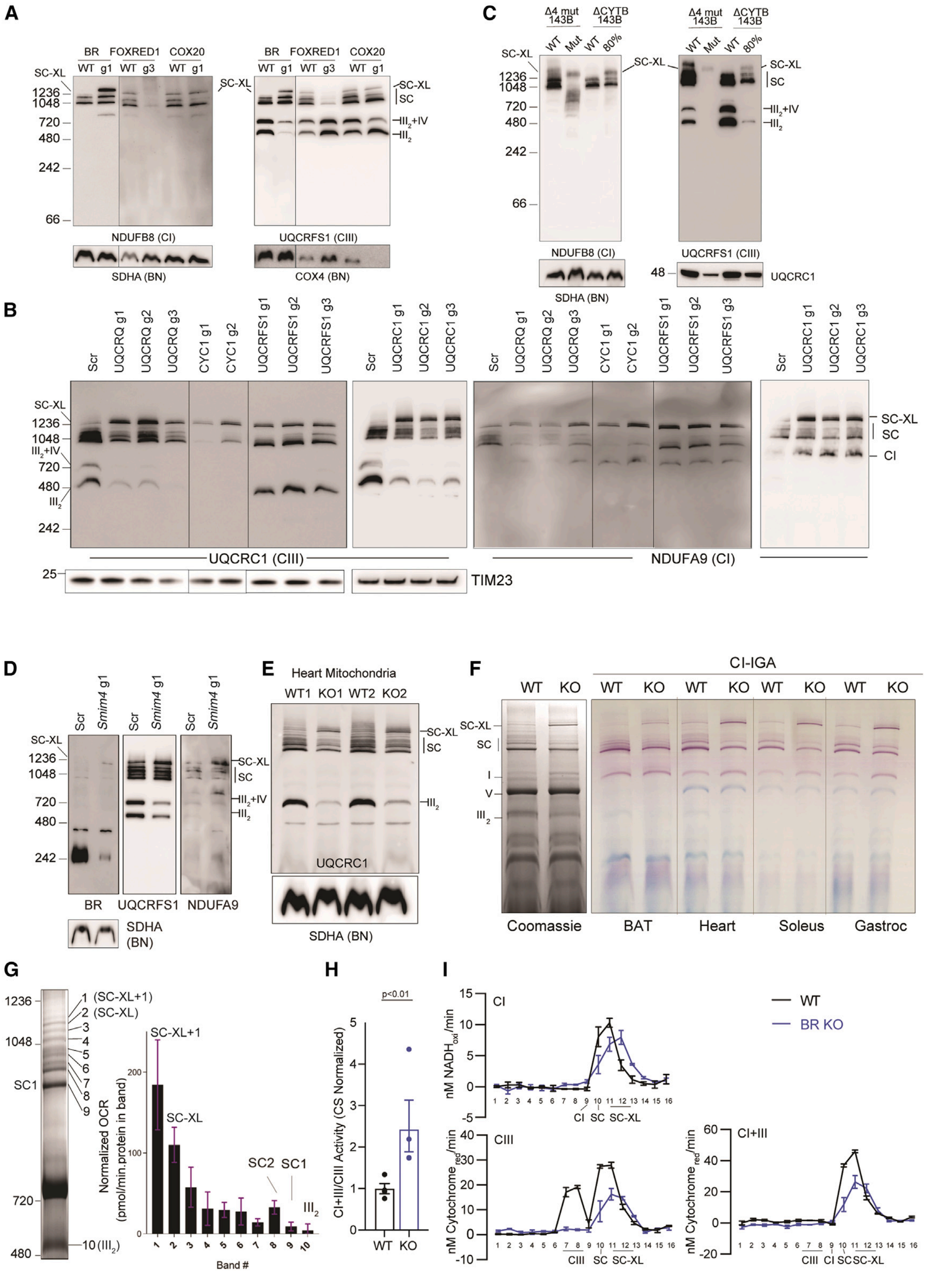

Figure 1. CIII deficiency triggers the formation of the SC-XL

(A) Western blots (WBs) of BN-PAGE for digitonin-extracted C2C12 mitochondria with FOXRED1, BR, and COX20 gRNAs.

(B) WBs of BN (top) and SDS-PAGE (bottom) for digitonin-extracted C2C12 mitochondria with UQCRQ, CYC1, UQCRFS1, and UQCRC1 gRNAs.

(C) WBs of BN and SDS-PAGE for digitonin-extracted 143B cybrid mitochondria with CYTB mutations (Δ4 mut, ΔCYTB), and WT isogenic mtDNA.

(D) WB-BN-PAGE of digitonin-extracted mitochondria with SMIM4 gRNA.

(E) WB-BN-PAGE of digitonin-extracted WT and BR KO murine cardiac mitochondria.

(legend continued on next page)

Please cite this article in press as: Liang et al., Formation of I$_2$+III$_2$ supercomplex rescues respiratory chain defects, Cell Metabolism (2024), https://doi.org/10.1016/j.cmet.2024.11.011

type, 85%–100% of CI, 55%–65% of CIII, and 15%–25% of CIV are found in SCs.[1] SCs can comprise two complexes, such as I+III$_2$[2] and III$_2$+IV,[3] or all three complexes, I+III$_2$+IV, termed a "respirasome."[4,5] Structural studies have identified non-conventional large respirasomes like the I$_2$+III$_2$+IV$_2$ "mega-complex" in 293T cells[6] and I+II+III$_2$+IV$_2$ in ciliates.[7] Although SCs have been known for over 20 years, their mechanisms and roles remain controversial. SCs may enhance oxidative phosphorylation (OXPHOS) by lowering reactive oxygen species (ROS) production,[8] increasing complex stability,[9,10] or providing catalytic advantages.[3,11] Some studies suggest that SCs may facilitate electron carrier transfer or enhance OXPHOS based on fuel availability by substrate channeling,[12–14] but these theories are debated due to evidence of an undifferentiated quinone pool.[15,16] Likewise, structural studies of SCs do not support direct carrier (cyt *c* or ubiquinone) transfer channels between complexes.[3] As such, the role of SCs in regulating OXPHOS efficiency remains unclear.

SC studies are challenging due to limited methods to modulate SC formation without affecting free ETC complexes. One exception was the discovery of SCAFI (COX7A2L/COX7RP), which promotes III$_2$+IV SC formation[12,17] by bridging CIII and CIV.[3] SCAFI expression rises during stress,[18] lipid-driven OXPHOS,[12] and infection.[19] SCAFI knockout (KO) mice show lower exercise tolerance,[20] suggesting a positive role of III$_2$+IV in respiration, even though SCAFI is not required for the formation of I+III$_2$+IV respirasomes.[3,21] However, using a mouse model missing the conserved EED motif in Uqcrc1 (*Uqcrc1*$^{del:E258\text{-}D260}$) in CIII, a key CI contact site,[22] Milenkovic et al. showed that severe reductions (75%–90%) in SCs did not cause discernible bioenergetic deficits, even during exercise. This calls into question the physiological requirement for SCs.

Similarly, the mechanisms underlying SC formation are unclear, though it is well-accepted that they form via stepwise association of ETC assembly intermediates rather than pre-formed complexes.[23] SC formation can vary by metabolic status[24] and be triggered by stressors like unfolded protein response,[18] DHODH (dihydroorotate dehydrogenase),[25] or SYK (spleen tyrosine kinase) inhibition,[26] suggesting it is adaptive for energy output regulation. Ugalde et al. showed that SCAFI (supercomplex assembly factor I or COX7A2L) and paralogs COX7A1/COX7A2 generate alternative respirasomes, S-MRC (mitochondrial respiratory chain) and C-MRC.[27] C-MRC has higher activity and is preferred when pyruvate dehydrogenase complex is activated, promoting OXPHOS, while metabolic shift toward glycolysis stabilizes the less active S-MRC.[27] SC formation *in vivo* is thus dynamic, stress-responsive, and may meet energy or oxidative demands. In *Drosophila*—which do not form respirasomes under basal conditions—SC formation occurs in response to defective ETC assembly,[28] indicating SCs may form under metabolic stress. Whether this is true in mammals is unclear.

Inspired by previous observations by Mootha and colleagues' findings that genetic ETC perturbations trigger protective compensatory mitochondrial adaptations,[29] we asked if ETC structural adaptations via SC formation are a means by which mitochondria can buffer against intrinsic stress. In this study, we searched for metabolic challenges sufficient to enhance the formation of SCs. We demonstrate that mutations that reduce but do not abolish the levels of CIII are sufficient to trigger the formation of an extra-large respirasome we termed the "SC-XL." The SC-XL has a stoichiometry of I$_2$+III$_2$ and effectively rescues respiratory defects caused by CIII insufficiency. Our work highlights the incredible plasticity of the ETC to overcome metabolic stress by functional rearrangements of respiratory complexes.

RESULTS

Inducible formation of a functional SC-XL by CIII deficiency

We hypothesized that partial inhibition of ETC complexes by knocking down assembly factors would trigger ETC structural adaptations. To this end, we knocked out a representative factor in each ETC complex—*Foxred1* for CI,[30,31] *Brawnin* (*Br*) for CIII,[32] and *Cox20* for CIV[33] in C2C12 mouse myoblasts (Figure 1A). While each KO reduced its target complex, only CIII perturbation (*Brawnin* KO [*BR* KO]) led to a large SC above conventional SCs, termed SC-XL (Figure 1A). Besides BR KO, CRISPR-Cas9-mediated knockdowns of other CIII subunits (*Uqcrq*, *Cyc1*, *Uqcrfs1*, and *Uqcrc1*) also induced SC-XL formation, often with reduced conventional CI and CIII-containing SCs (Figure 1B). Graded knockdown of CIII core subunit *Uqcrc1* using siRNAs showed that a 60% mRNA reduction was enough to trigger SC-XL formation (Figure S1A). In line with previous observations,[34] human cybrids with *mt-Cyb* mutations also formed a similar SC-XL (Figure 1C). SC-XL was likewise observed in *UQCRH* mutant patient fibroblasts and *Uqcrh* KO mouse.[35] Intriguingly, induction of a SC-XL-like SC by CIII deficiency is also observed in *Drosophila*,[28] suggesting that SC-XL formation in response to ETC stress is conserved across species. Of note, a residual CIII level is required for SC-XL formation since mutants lacking nearly all CIII (e.g., *Cyc1* KOs) show reduced SC-XL (Figure 1B) due to CI destabilization.[36]

BR is required for early CIII assembly. Together with its obligate partner SMIM4 (small integral membrane protein 4 or UQCC5), BR forms the COMB that mediates CYTB maturation.[37] *Smim4*, when knocked out, also induced SC-XL in C2C12 cells (Figure 1D), supporting the use of the BR/SMIM4 (UQCC5/6) manipulation to study SC-XL. Hereafter, we proceeded to use BR KO as the perturbation of choice to induce SC-XL formation. We then asked if SC-XL is formed *in vivo* by examining cardiac mitochondria from BR KO mice,[37] which revealed a 50%–60% downregulation of CIII subunits (Figures S1B and S1C), leading

(F) Coomassie staining (left) and complex I in-gel activity (IGA, right) on BN-PAGE of WT and BR KO murine mitochondria from various tissues (brown adipose tissue [BAT], heart, soleus, gastrocnemius).

(G) Oxygen consumption of BN-PAGE bands from BR KO murine cardiac mitochondria in Seahorse assay, normalized to protein levels by Coomassie staining. Band 2 = SC-XL.

(H) Ratio of respiratory complex I+III to complex III activity in WT and BR KO cardiac mitochondria. Data as mean ± SEM, *n* = 3, with *p* values from two-tailed unpaired t tests.

(I) Respiratory complex activities (CI, CIII, CI+CIII) of WT and BR KO cardiac mitochondria across sucrose gradient fractions, normalized by total protein.

Please cite this article in press as: Liang et al., Formation of I_2+III_2 supercomplex rescues respiratory chain defects, Cell Metabolism (2024), https://doi.org/10.1016/j.cmet.2024.11.011

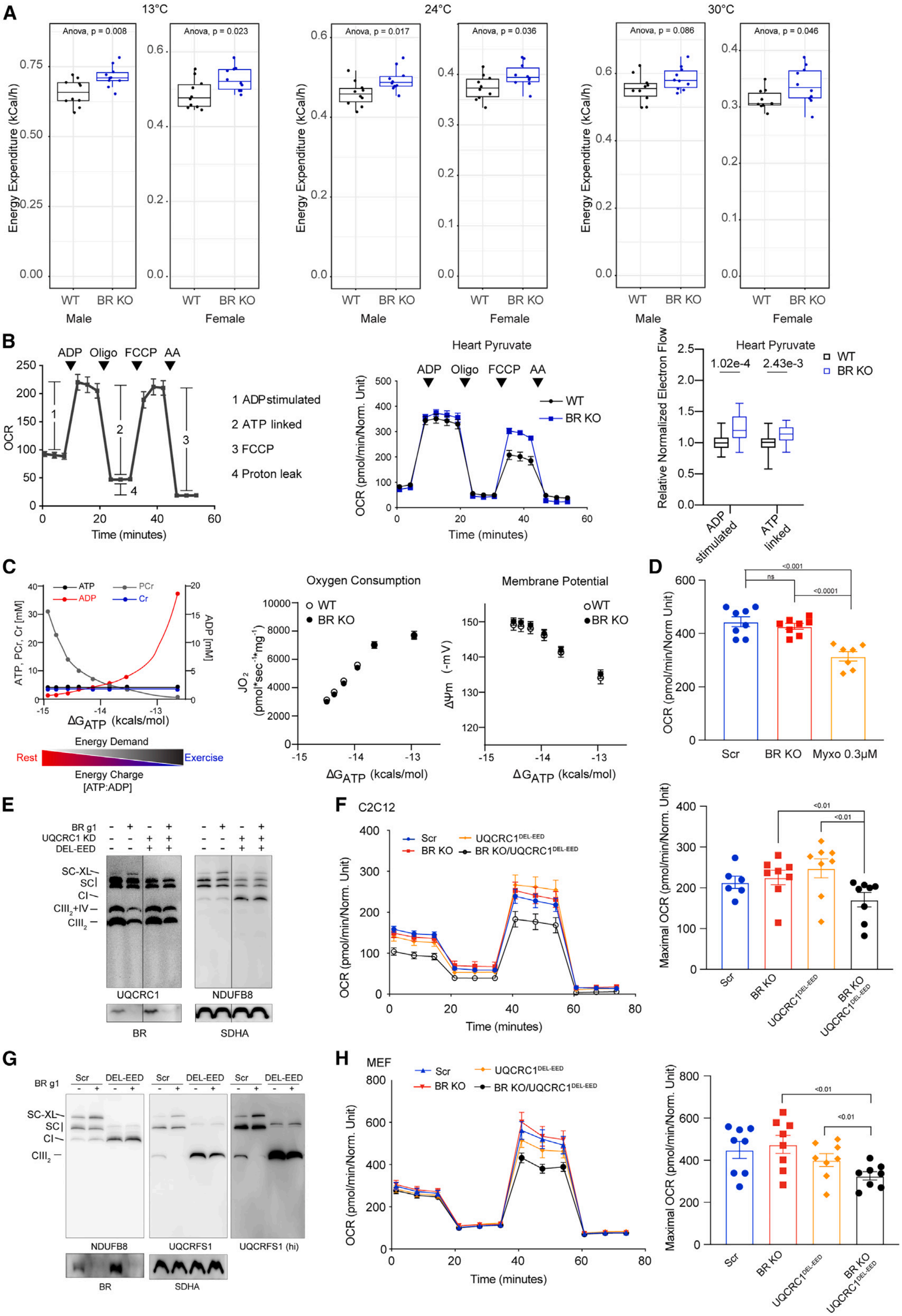

Figure 2. SC-XL compensates for CIII deficiency

(A) Whole-body energy expenditure (EE) in WT and BR KO mice of both sexes measured by indirect calorimetry under cold (13°C), room temperature (24°C), and thermoneutral (30°C) conditions. p values from ANOVA of weight-adjusted EE. Data as mean ± SEM, $n = 10$.

(legend continued on next page)

Please cite this article in press as: Liang et al., Formation of I_2+III_2 supercomplex rescues respiratory chain defects, Cell Metabolism (2024), https://doi.org/10.1016/j.cmet.2024.11.011

to a ~70% reduction in CIII activity (Figure S1D). Indeed, BN (blue-native)-PAGE analysis revealed that the SC-XL was formed very prominently in BR KO cardiac mitochondria (Figure 1E). Two-dimensional BN-SDS-PAGE analysis showed that the SC-XL contains CI and CIII subunits, along with a weak signal for CIV subunit COX1 (Figure S1E). Therefore, SC-XL formation is triggered both *in vitro* and *in vivo* upon challenge with a severe but not complete CIII deficiency.

SC-XL is functional and competent to respire

While formation of smaller complexes resulting from stalled assembly intermediates is commonly observed in ETC mutants, formation of larger complexes is rare and poorly investigated. The SC-XL could either be an aggregate of non-functional complexes or a functional and higher-order SC formed in mitigative response to respiratory deficits caused by CIII deficiency. To determine if the observed SC-XL is indeed a functional respirasome, we measured CI activity in SC-XL from tissues using an in-gel assay and confirmed its NADH dehydrogenase enzymatic activity (Figure 1F). We then measured the oxygen consumption of BN-PAGE gel slices on the Seahorse and found that the SC-XL indeed exhibited detectable oxygen consumption in response to NADH and marginally higher respiration rates per unit of protein compared with smaller SCs (Figure 1G). Sucrose gradient fractionation of digitonin-solubilized mitochondrial lysates furthermore showed SC-XL fractions had higher I+III_2 activity in KO than wild type (WT), normalized to total CIII (Figure 1H). Furthermore, CI, CIII, and CI+III activities shifted to the SC-XL region in BR KO mitochondria (Figures 1I and S1F). Exercise in mice increased SC-XL levels (Figure S1G), aligning with prior studies linking SC formation in humans with exercise.[38] Differentiation of C2C12 cells into myotubes, associated with a metabolic shift toward OXPHOS,[39] also favored SC-XL (Figure S1H), suggesting that the SC-XL is functional under physiological conditions and is induced by increased OXPHOS demand. Altogether, our data indicate that in BR KO mitochondria, a functional SC-XL respirasome forms in place of free III_2.

SC-XL rescues bioenergetic defects of CIII deficiency in BR KO mice

We hypothesized that SC-XL forms to buffer against the respiratory effects of reduced CIII activity. While BR KO zebrafish develop lethal mitochondrial disease with growth retardation, reduced motility, and lactic acidosis,[32] BR KO mice were surprisingly asymptomatic except for mild exercise intolerance,[37] with normal growth (Figure S2A), body mass (Figure S2B), and muscle succinate levels (Figure S2C). Importantly, in our hands, we did not detect appreciable levels of SCs in WT or BR KO zebrafish,[32] suggesting that their severe phenotype might be due to the inability to buffer their respiratory chain with the SC-XL.

Using indirect calorimetry, we found that BR KO animals had normal to higher energy expenditure than WT animals at all temperatures (Figure 2A), despite a ~70% reduction in total CIII activity (Figure S1D). To understand if bioenergetic changes could instead be detected at the level of the mitochondria, we performed conventional Seahorse assays with isolated cardiac mitochondria fueled by pyruvate/malate. Consistent with indirect calorimetry on an organismal level, BR KO mitochondria had slightly elevated rates of respiration compared with WT (Figure 2B). Intriguingly, despite reduced electron flow through CIV (Figure S2D), overall flow through CI-III-IV or CII-III-IV was normal in BR KO mitochondria, suggesting increased flow through CI+III_2. However, since these experiments were performed under conditions of excess fuel and ADP, they may mask a partial defect in BR KO. We therefore turned to the comprehensive respirometric Oroboros-based diagnostics platform developed by Muoio and colleagues,[40] which serves as an *in vitro* "stress test" of mitochondrial competence to meet physiologically relevant energy demands. By measuring the relationship between energy demand (ATP:ADP) and oxygen consumption (JO2), this platform estimates respiratory conductance, a proxy of ETC efficiency and competence.[40] Likewise, this analysis revealed that BR KO mitochondria were not impaired in respiratory conductance in response to pyruvate (Figure 2C). In fact, BR KO mitochondria were able to maintain a higher membrane potential compared with WT mitochondria in some fuels such as succinate and palmitoyl-carnitine (Figure S2E). Hence, despite a 70% reduction in CIII activity, BR KO mitochondria have normal bioenergetic output. These data suggest that BR KO mitochondria are protected against the respirometric defects arising from a severe deficiency in CIII, potentially due to SC-XL formation.

To understand the mechanistic basis of the observed respirometric rescue in BR KO, we turned to the murine C2C12 myoblast model.[37] Consistent with studies in BR KO mice and tissues, BR KO C2C12 myoblasts have normal respiration (Figure 2D). One possible explanation is that the residual CIII activity in BR KO cells can still support levels of OXPHOS. To define the threshold of CIII activity required for normal respiration, we titrated C2C12 myoblasts with myxothiazol, a reversible CIII inhibitor that binds to the Qo CoQ-binding site of CIII to inhibit its activity without generating substantial ROS.[41] C2C12 treated with 300 nM of myxothiazol and BR KO C2C12 had the same reduction in CIII electron (i.e., 15%) (Figure S2F). While BR KO

(B) Oxygen consumption rate (OCR) in WT and KO cardiac mitochondria measuring pyruvate-stimulated electron flow. ADP-stimulated and ATP-linked uncoupled OCR (left), with relative activity to WT (right). Data as mean ± SEM, $n = 8$.

(C) (Left) Schematic of metabolite changes and ATP hydrolysis free energy (ΔGATP) in creatine kinase (CK) clamp simulating rest-to-exercise transition. (Right) Phosphocreatine titration in WT and BR KO cardiac mitochondria with pyruvate/malate, coupled to oxygen consumption (JO2) or membrane potential ($\Delta\psi$).

(D) Basal and maximal oxygen consumption of C2C12 cells with scramble gRNA, BR g1, or 0.3 μM myxothiazol. Data as mean ± SEM, $n = 8$.

(E) BN-PAGE WB of digitonin-extracted mitochondria from C2C12 cells expressing Scr, BR g1, UQCRC1 g1-3, and/or UQCRC1DEL-EED.

(F) OCR of C2C12 cells expressing Scr, BR g1, and/or UQCRC1DEL-EED. Seahorse trace (left) and basal/maximal OCR quantification (right). Data as mean ± SEM, $n = 8$.

(G) BN-PAGE WB of digitonin-extracted mitochondria from WT and UQCRC1DEL-EED MEFs expressing Scr or BR gRNAs.

(H) OCR of MEFs from WT and UQCRC1DEL-EED mice with Scr or BR gRNAs. Seahorse trace (left) and basal/maximal OCR quantification (right). Data as mean ± SEM, $n = 8$.

All p values are from two-tailed unpaired t test, unless otherwise stated.

Please cite this article in press as: Liang et al., Formation of I_2+III_2 supercomplex rescues respiratory chain defects, Cell Metabolism (2024), https://doi.org/10.1016/j.cmet.2024.11.011

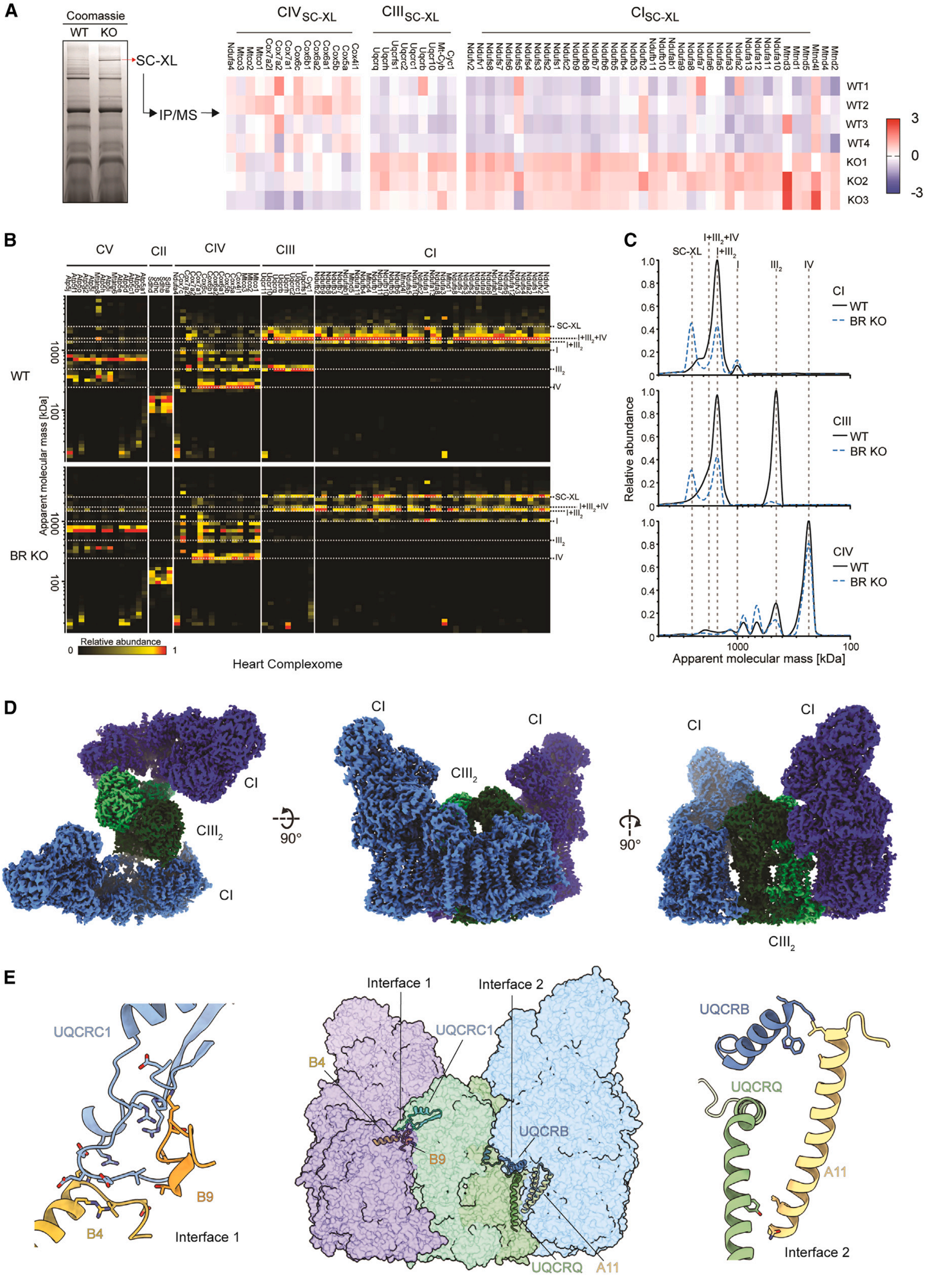

(legend on next page)

C2C12 had normal respiration, 300 nM of myxothiazol substantially reduced oxygen consumption (Figure 2D) because myxothiazol did not induce compensatory SC-XL formation (Figure S2G). Therefore, we posited that CIII deficiency in BR KO animals is asymptomatic due to the compensatory formation of the SC-XL. If this model is correct, disrupting SC-XL formation in BR KO cells should cause respiratory decompensation. A recent study by Larsson and colleagues found that deletion of the amino acids $EED^{258–260}$ in UQCRC1—a structural subunit of CIII—leads to the disassembly of SCs without affecting the levels of individual ETC complexes.[22] $UQCRC1^{E258\text{-}D260}$ is in a conserved loop where CIII forms a critical contact point with NDUFB4 in CI to facilitate SC formation. We therefore expressed $UQCRC1^{DEL:E258\text{-}D260}$ together with knockdown of endogenous WT UQCRC1 in BR KO C2C12 cells (hereafter referred BR KO; $UQCRC1^{DEL\text{-}EED}$) to recapitulate the homozygous $UQCRC1^{DEL:E258\text{-}D260}$ knockin mutation by the Larsson lab. As anticipated, BR KO; $UQCRC1^{DEL\text{-}EED}$ C2C12 had reduced SC-XL and concomitant increase in free CI and CIII dimers (Figure 2E). Consequently, BR KO; $UQCRC1^{DEL\text{-}EED}$ C2C12 had significantly reduced respiration compared with BR KO C2C12 (Figure 2F), even though CIII activity was unchanged (Figure S2H). In a reciprocal experiment, we deleted BR in mouse embryonic fibroblast (MEF) derived from $UQCRC1^{DEL:E258\text{-}D260}$ knockin mice.[22] Similarly, BR KO in $UQCRC1^{DEL:E258\text{-}D260}$ MEF abrogated SC and SC-XL formation (Figure 2G) and significantly reduced maximal respiration compared with BR KO alone (Figure 2H), despite unchanged CIII activity (Figure S2I). Furthermore, we serendipitously isolated a clone of BR KO C2C12 cells that lost the formation of the SC-XL (Figure S2J), without changes in CIII activity (Figure S2K). We refer to these cells as "NS" or "no SC-XL" cells, with its matched WT control as "Scr NS." Similar to $UQCRC1^{DEL:E258\text{-}D260}$ cells, BR KO-NS had reduced maximal respiration, revealing the expected phenotype of CIII deficiency in the absence of SC-XL (Figure S2L). These data suggest that the SC-XL enables the same level of energy output for a reduced amount of CIII, thereby increasing the efficiency of the ETC as defined by energy output per ETC complex. In the absence of the SC-XL, as in the $UQCRC1^{DEL:E258\text{-}D260}$ or "NS" background, cells with CIII deficiency become decompensated and exhibit respiratory deficits.

The SC-XL is a I_2+III_2 SC

To define the biochemical composition of the SC-XL, we excised the SC-XL from a BN-PAGE gel for liquid chromatography-mass spectrometry (LC-MS/MS) label-free quantitation (Figure 3A; Table S1). The SC-XL band contains components of CI, CIII, and CIV, although spectral intensity from CI and CIII subunits was higher in KO compared with WT (Figures 3A and S3A; Table S1), indicating that the SC-XL is dominated by CI and CIII. BN-PAGE of DDM solubilized and excised SC1 (I+III_2), SC2 (I+III_2+IV), and SC-XL confirmed the SC-XL contains a significantly lower content of CIV compared with SC2 (Figure S3B), resembling SC1 in composition.

To clarify the stoichiometry of the SC-XL, we performed complexome analysis, which allows us to compare the SC-XL with other conventional SCs of known composition (Figure S3C).[42] This analysis confirmed that BR KO mitochondria lost free CIII dimers and rearranged their SCs, losing smaller respirasomes and preferentially formed the SC-XL of approximately 2.8 MDa (Figures 3B, 3C, and S3B; Table S1). Of note, the SC-XL migrates on a BN-PAGE at the 1.2 MDa marker, and this discrepancy is likely due to differences in charge, conformation, Coomassie dye affinity, etc. between ETC proteins and that of the markers. By comparing the average normalized iBAQ (intensity-based absolute quantification) value of each ETC complex between the SC-XL (band 40) and the reference SC I+III_2+IV "SC2" (band 37), the estimated stoichiometry of the SC-XL is I_2+$III_{2.3}$+$IV_{0.2}$, suggesting it is a dimer of CI and CIII (i.e., I_2+III_2) with substoichiometric levels of CIV (Figure S3D; Table S1). Hence, the SC-XL has a higher CI but lower CIV content compared with conventional SC2 respirasomes.

The sub-stoichiometric presence of CIV—which is incongruent with our knowledge of how SC structure—suggests that these biochemical measurements are approximations at best, prone to inaccuracies due to contamination from co-migrating bands. To definitively define the structure and composition of the SC-XL, we isolated SC-XL from BR KO mouse heart mitochondria on a sucrose gradient (Figure S3E) and solved its structure to a nominal resolution of 3.7 Å using single-particle cryogenic electron microscopy (cryo-EM; Figures 3D, 3E, and S4; Video S1). This structure demonstrated that SC-XL is formed by two copies of CI surrounding one CIII dimer, confirming the overall stoichiometry of I_2+III_2. The structure also showed that both CIs and $CIII_2$ contain their full complement of 45 and 22 subunits, respectively. No additional subunits were observed in SC-XL. Minor classes of SC I+III_2+IV and I+III_2 were isolated during 3D classification of the particle images, indicating their presence in the pooled fractions, but no cryo-EM density consistent with a bound CIV was observed in the SC-XL reconstruction (Figures 3D and 3E). This suggests that the respiratory activity of excised SC-XL BN-PAGE bands (Figure 1G) is enabled by co-migrating or transiently interacting CIV rather than SC-XL-bound CIV. The individual complexes within SC-XL are consistent at the level of the resolution with known structures of mouse CI[43,44] and CIII,[3] indicating that no large-scale conformational

Figure 3. SC-XL is composed of two copies of CI surrounding a CIII dimer

(A) Mass spectrometry of SC-XL band excised from WT and BR KO digitonin-solubilized murine cardiac mitochondria on BN-PAGE. Coomassie staining (left) and BR KO/WT fold change analysis (right).

(B) Complexome heatmap showing protein levels of ETC complex subunits (normalized iBAQ values). Detailed slicing in Figure S3C.

(C) ETC complex abundance (CI, CIII, CIV) across 48 slices from high to low molecular weight, approximated by average normalized iBAQ values of constituent subunits (assembly factors excluded).

(D) Cryo-EM density of isolated SC-XL, with CI protomers in blue shades and CIII protomers in green shades, viewed from the mitochondrial matrix (left), CI side (middle), and CIII2 side (right).

(E) SC-XL major interfaces on overall structure (center). Interface 1: CI subunits NDUFB4/NDUFB9 and CIII subunit UQCRC1 in the mitochondrial matrix (left). Interface 2: CI subunit NDUFA11 and CIII subunits UQCRB/UQCRQ in the inner mitochondrial membrane.

Please cite this article in press as: Liang et al., Formation of I_2+III_2 supercomplex rescues respiratory chain defects, Cell Metabolism (2024), https://doi.org/10.1016/j.cmet.2024.11.011

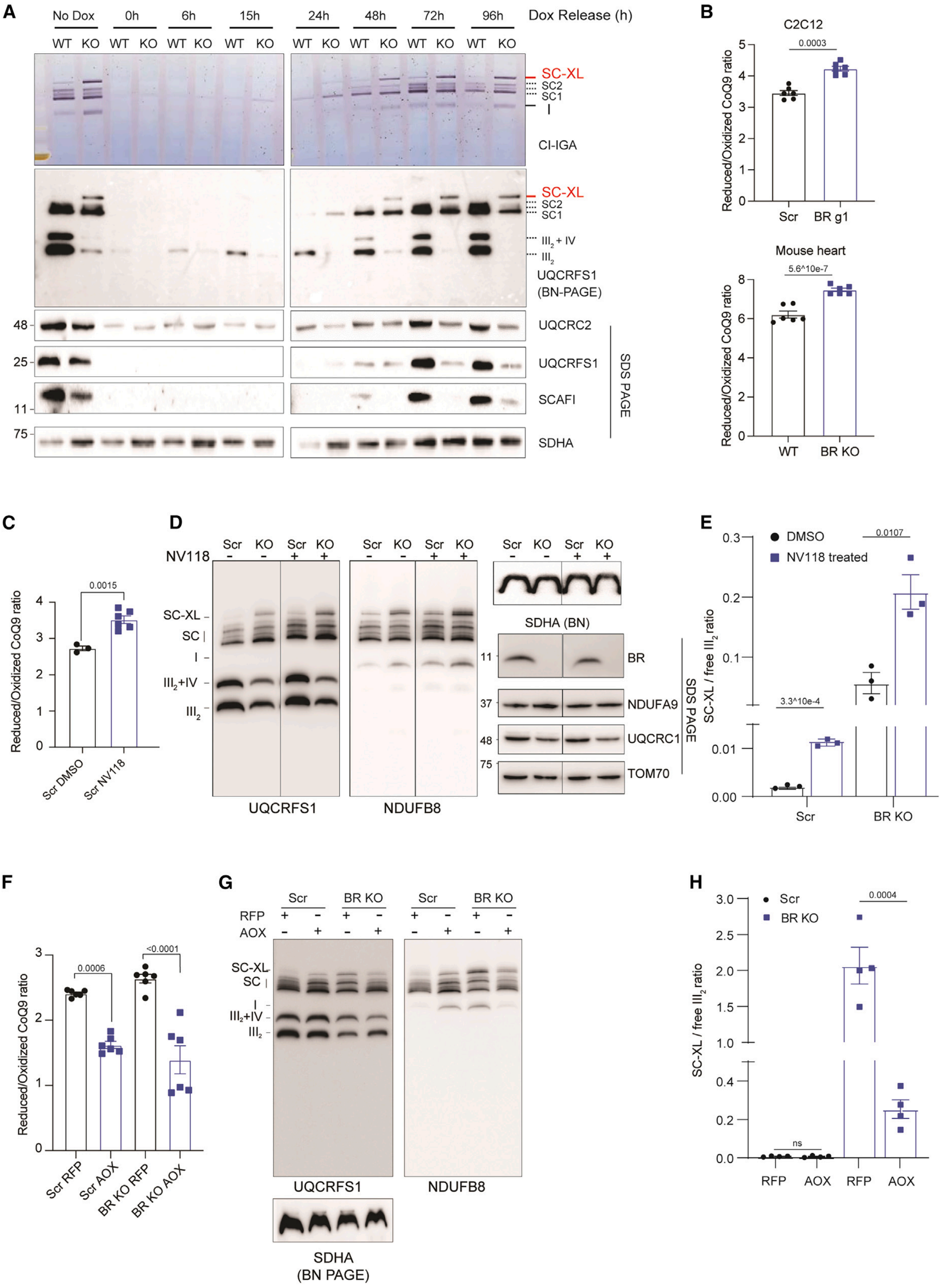

(legend on next page)

Please cite this article in press as: Liang et al., Formation of I$_2$+III$_2$ supercomplex rescues respiratory chain defects, Cell Metabolism (2024), https://doi.org/10.1016/j.cmet.2024.11.011

changes are needed to favor SC-XL formation. The contact sites between both CIs and the CIII dimer are consistent with what is seen in the ovine SC I+III$_2$. These data demonstrate that SC-XL can form without major structural or compositional changes in the constituent complexes, suggesting that the formation of SC-XL is either driven passively by the inherent affinity between CI and CIII under conditions where III$_2$ becomes limiting or by other metabolic, membrane, or bioenergetic mechanisms.

Structural studies have suggested that the CIII dimer within I+III$_2$+IV SCs is functionally asymmetrical,[2,3,5] with potentially only one active protomer specializing in CoQH$_2$ (coenzyme Q-reduced or ubiquinol) oxidation proximal to CI and CoQ (coenzyme Q-oxidized or ubiquinone) reduction proximal to CIV.[45] In SC I+III$_2$+IV, symmetry breaking of CIII by its interactions with CI and CIV has been proposed to functionally split the Q-cycle activity within the III$_2$ dimer. In this scenario, the CIII Q-cavity adjacent to CI is specialized for CoQH$_2$ oxidation, and the Q-cavity adjacent to CIV is specialized for CoQ reduction.[46] This symmetry breaking has been observed at the level of the Rieske FeS head domain of subunit UQCRFS1, which must undergo conformational changes to transfer an electron between CoQH$_2$ and cyt c_1.[47] In an early structural study of the respirasome from bovine cardiac tissue,[5] clear cryo-EM density was observed for the Rieske FeS head domain adjacent to CIV, indicating trapping in a single position and an inability to transfer electrons, suggesting the Q-cavity adjacent to CIV would be incapable of CoQH$_2$ oxidation. While in the same structure, the cryo-EM density for the FeS head domain adjacent to the CI Q-tunnel was weak and diffuse, indicating flexibility and suggesting that the Q-cavity adjacent to CI would be competent for electron transfer from CoQH$_2$ to cyt c. In our structure of the nearly symmetric SC-XL, we do not see any notable difference in the cryo-EM density for the two Riske FeS head domains (Figure S3F), even after focused refinement around the symmetry-breaking Sub9 (Uqcrfs1n), suggesting that III$_2$ within SC-XL might be functionally symmetric with both protomers capable of both CoQH$_2$ oxidation and CoQ reduction.

SC-XL formation is driven by CoQH$_2$ accumulation secondary to partial CIII deficiency

We next sought to decipher the mechanisms that stimulate the SC-XL formation, hypothesizing that it is enabled by preferential association between CI and CIII when CIII subunits are in short supply. By examining the kinetics of SC-XL formation using a doxycycline pulse-chase experiment (Figure 4A), we verified that nascent CIII indeed preferentially associates with CI, assembling first into I+III$_2$ and then into SC-XL in BR KO C2C12. As such, high levels of CI are likely to be a pre-requisite for SC-XL formation, and BR KO "NS" cells probably lost the SC-XL due to a reduction in CI subunits (Figure S5A). One reason for increased CI and CIII association could be the reduced CIII and CIV association, since SCAFI expression is severely downregulated in BR KO heart (SCAFI^{111}) (Figure S5B) and C2C12 (SCAFI^{113}) (Figure S5C). However, forced expression of SCAFI^{113} in BR KO heart (Figure S5D) or in BR KO C2C12 (Figure S5E) was not sufficient to reverse SC-XL formation, suggesting that the downregulation of SCAFI is not the reason for SC-XL formation.

Another potential trigger for SC-XL formation is elevated CoQH$_2$/CoQ ratio, a consequence of CIII deficiency. CoQH$_2$/CoQ has previously been implicated as a sensor for the formation of SCs.[48] In this model, very high CoQH$_2$/CoQ ratios drive reverse electron transport (RET) to cause CI degradation and dissociation of SCs. However, whether milder elevations of CoQH$_2$/CoQ ratios will trigger homeostatic mechanisms such as SC-XL formation is unknown. As expected of partial CIII functional deficit, CoQH$_2$/CoQ ratios in BR KO C2C12 and mouse heart mitochondria were mildly elevated (Figure 4B). We elevated CoQH$_2$/CoQ ratio in WT C2C12 cells to the same extent as seen in BR KO by administering a cell-permeable analog of succinate, NV118 (Figure 4C). This was sufficient to increase the formation of SC-XL in WT cells and even in BR KO cells (Figures 4D and 4E), suggesting that elevated CoQH$_2$/CoQ could be a signal for increasing CI and CIII association. If so, dampening the elevated CoQH$_2$/CoQ ratio in BR KO should reverse SC-XL formation. To this end, we expressed the alternative oxidase (AOX) from *Ciona intestinalis*[49] which re-oxidizes excess CoQH$_2$ in BR KO C2C12. Indeed, AOX expression restored the CoQH$_2$/CoQ ratio in BR KO (Figure 4F) and was sufficient to reduce the levels of SC-XL in BR KO but not in WT C2C12 (Figures 4G and 4H). Altogether, these data suggest that CoQH$_2$ accumulation might be the trigger for SC-XL formation. Of note, only mild CoQH$_2$/CoQ elevation is compatible with SC-XL formation. Myxothiazol treatment causes a large (7.5-fold) over-reduction of CoQH$_2$ (Figure S5F), which prevents SC-XL formation (Figure S2G) potentially due to complete inhibition of CI electron flow and generation of CI ROS.

SC-XL reduces CI and CIII ROS production and enhances mitochondrial integrity

We next sought to address the potential benefits of SC-XL formation on mitochondrial bioenergetics. CI and CIII are the major sites of mitochondrial ROS production (Figure S6A), and respirasomes are proposed to enhance electron transfer and reduce

Figure 4. SC-XL formation is driven by CoQH$_2$ accumulation secondary to partial CIII deficiency

(A) BN-PAGE and SDS-PAGE of C2C12 mitochondria from Scr and BR g1 cells after 8-day doxycycline pulse and subsequent washout for ETC reassembly. BN-PAGE CI in-gel activity (IGA, top), BN-PAGE WB with anti-UQCRFS1 (middle), and SDS-PAGE WBs with anti-UQCRC2, UQCRFS1, SCAF1, and SDHA (loading control).

(B) Reduced/oxidized CoQ$_9$ analysis in C2C12 cells with Scr or BR gRNA1 (top) and in WT/KO mouse heart tissues (bottom). Data as mean ± SEM, $n = 6$.

(C) Reduced/oxidized CoQ$_9$ analysis in C2C12 cells with Scr gRNA treated with 100 μM NV118 for 24 h. Data as mean ± SEM, $n = 3$ (DMSO) or 6 (NV118).

(D) BN-PAGE WB of C2C12 mitochondria with Scr or BR gRNA1 treated with DMSO or NV118 (24 h).

(E) SC-XL to free III2 ratio shown in (D). Data as mean ± SEM, $n = 3$.

(F) Reduced/oxidized CoQ$_9$ analysis in C2C12 cells with Scr or BR gRNA and control RFP (red fluorescent protein) or AOX overexpression. Data as mean ± SEM, $n = 6$; p values from two-tailed unpaired t test.

(G) BN-PAGE of C2C12 mitochondria with Scr or BR gRNA1 and control RFP or AOX overexpression.

(H) SC-XL to free III2 ratio shown in (G). Data as mean ± SEM, $n = 4$.

All p values are from two-tailed unpaired t test.

Please cite this article in press as: Liang et al., Formation of I_2+III_2 supercomplex rescues respiratory chain defects, Cell Metabolism (2024), https://doi.org/10.1016/j.cmet.2024.11.011

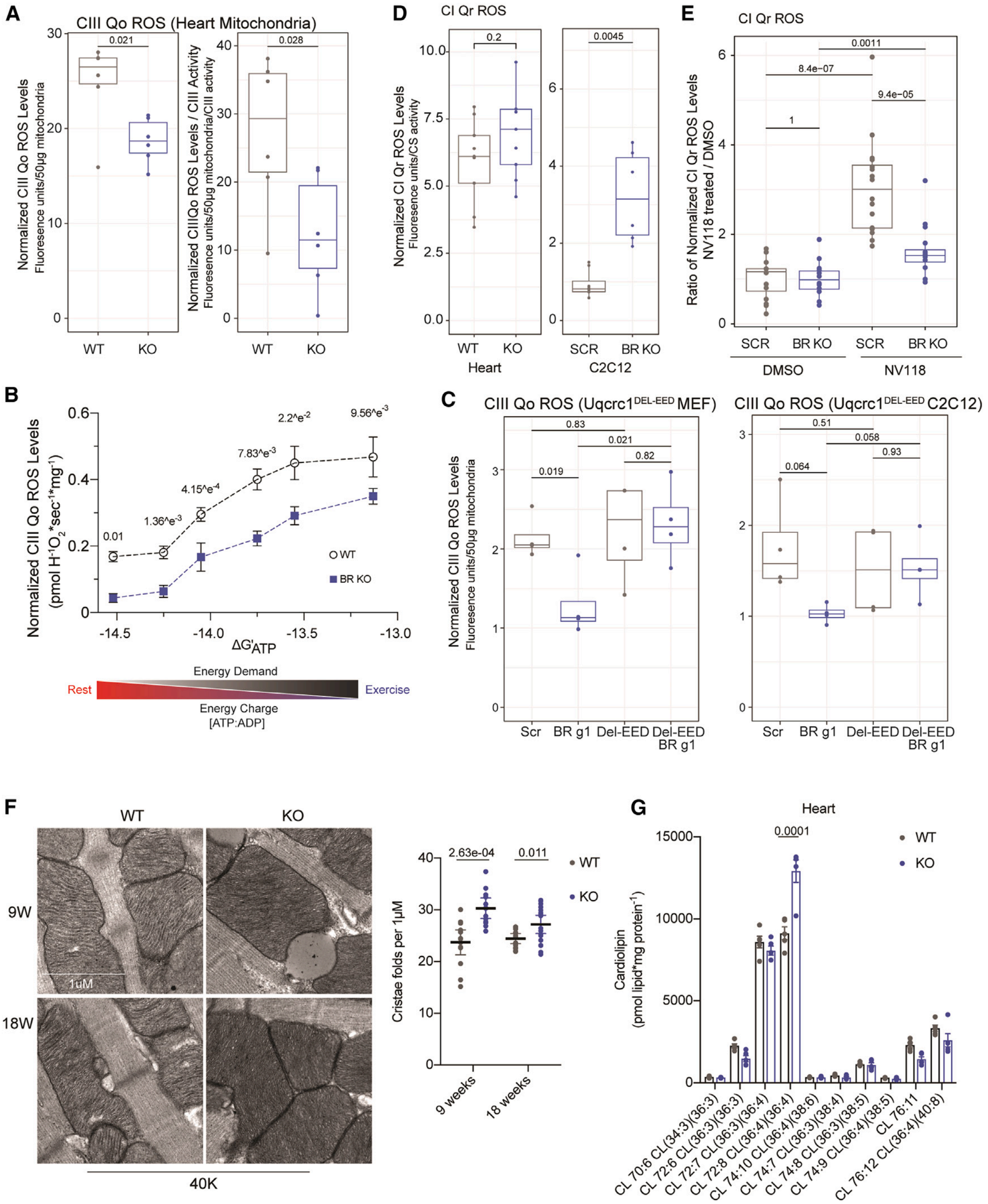

Figure 5. SC-XL produces less ROS and enhances mitochondrial integrity

(A) ROS emission at CIII QO site in WT and BR KO murine cardiac mitochondria, normalized to mitochondrial amount (left) and CIII activity (right). Data as mean ± SEM, *n* = 6.

(B) ROS emission at CIII QO site during creatine kinase (CK) clamp and phosphocreatine titration in WT and BR KO cardiac mitochondria with succinate. Data as mean ± SEM, *n* = 4.

(C) ROS emission at CIII QO site in UQCRC1DEL-EED MEFs (left) and C2C12 cells (right) with Scr or BR gRNAs. Data as mean ± SEM, *n* = 6.

(D) Reverse electron transport (RET) ROS at CI in WT and BR KO cardiac mitochondria and Scr or BR KO C2C12 cells. Data as mean ± SEM, *n* = 6.

(E) RET-induced ROS at CI in Scr or BR KO C2C12 cells. Relative fold change of RET ROS in cells treated with NV118 (100 µM) vs. DMSO. Data as mean ± SEM, *n* = 12.

(legend continued on next page)

Please cite this article in press as: Liang et al., Formation of I_2+III_2 supercomplex rescues respiratory chain defects, Cell Metabolism (2024), https://doi.org/10.1016/j.cmet.2024.11.011

electron leak and ROS,[8,50] although in our opinion, this point has not been sufficiently demonstrated in the literature. Despite the CIII defect in BR KO cells, which is expected to increase ROS production, we found that BR KO C2C12 cells in fact had reduced total mitochondrial ROS as measured by mitoSOX staining (Figures S6B and S6C), as well as reduced SOD1/2 levels (Figure S1B), indicating a lower ROS burden. ROS produced from different sites have different biological and pathological effects.[51,52] To assess how SC-XL alters mitochondrial ROS, we quantified ROS production from individual sites in CI and CIII using Amplex UltraRed assays coupled with specific inhibitors to pinpoint ROS production at distinct sites (Figure S6A).[53,54] This analysis revealed a significantly reduced production of ROS from the Q_o site of CIII in BR KO cardiac mitochondria, which trended lower even after normalizing for the reduced CIII activity (Figure 5A). CIII ROS reduction was observed under a wide range of energy demand levels simulated by the phosphocreatine clamp (Figure 5B), even at the highest demand level where mitochondria are carrying out coupled respiration at maximal capacity. We infer from these data that CIII in the SC-XL produces less Q_o ROS per unit of ubiquinone-reducing activity compared with free CIII. Consistently, BR KO; UQCRC1$^{DEL\text{-}EED}$ C2C12 and MEF (Figure 5C) as well as BR KO "NS" cells (Figure S6D) that have lost the SC-XL all had higher levels of CIII Q_o ROS. These data support the conclusion that CIII in the SC-XL is more efficient as defined by lower CIII ROS production. Succinate accumulation and increased $CoQH_2$/CoQ ratio in BR KO are predicted to enhance RET and CI ROS (i.e., CI_{Qr} ROS).[55] Indeed, under basal conditions, both C2C12 and cardiac BR KO mitochondria showed a small but significant increase in CI_{Qr} ROS (Figure 5D), while CI_{Ff} ROS in the forward direction was not significantly affected (Figure S6E). However, when C2C12 myoblasts were treated with the succinate analog NV118—which triggers CI_{Qr} ROS by elevating $CoQH_2$—BR KO cells have reduced induction of CI_{Qr} ROS compared with WT cells (Figure 5E). This suggests that the SC-XL can buffer against a surge in CI_{Qr} ROS. Consistent with this, we found that BR KO cardiac mitochondria had enhanced coupling to respiration fueled by succinate and a significantly lowered rate of uncoupled activity or proton leak (Figure S6F). Altogether, these results demonstrate that BR KO cells in the presence of SC-XL have reduced mitochondrial CIII ROS production and—potentially due to enhanced coupling to succinate-driven respiration—are protected against RET ROS generated at CI_Q during surges in succinate-fueled respiration.

An improved redox environment predicts that BR KO will have improved mitochondrial integrity. Indeed, BR KO cardiac muscle had a higher mitochondrial DNA (mtDNA) copy number compared with WT (Figure S6G) and significantly increased cristae density (Figure 5F). Consistent with increased cristae and SC-XL formation, BR KO cardiac mitochondrial membranes had significantly higher levels of tetra-linoleoyl cardiolipin (TLCL) (Figure 5G), the mature form of cardiolipin that is required for ETC function and known to potentiate SC formation by bridging interfaces between individual complexes.[56] These results demonstrate that consistent with enhanced bioenergetics, SC-XL formation is corelated with structural remodeling of cristae to maximize OXPHOS efficiency and output.

SC-XL is associated with metabolic reprogramming toward FAO

ETC ROS production is known to contribute to oxidative damage of mitochondrial proteins via post-translational modifications such as cysteine oxidation and carbonylation. We hypothesized that reduced CIII ROS in BR KO mitochondria might lead to reduced oxidative damage of proteins in the fatty acid oxidation (FAO) pathway, which was found to be specifically targeted by CIII ROS.[51] Indeed, treatment of C2C12 cells with S3QEL, which suppresses $CIII_{Qo}$ site ROS,[57] significantly increased FAO rate as measured by ^{14}C-palmitic acid FAO[58] (Figure S7A), supporting the hypothesis that CIII ROS impacts FAO. Additionally, multiple enzymes involved in FAO (e.g., HADHA and HADHB) are elevated in BR KO heart and C2C12 mitochondria (Figures 6A and S7B), consistent with their increased stability. Consequently, the rate of FAO was increased in both BR KO cardiac mitochondria (Figure 6B) and C2C12 myoblasts (Figure S7C). Notably, this observed increase in FAO was abrogated in BR KO; UQCRC1$^{DEL\text{-}EED}$ MEF (Figure 6C) and C2C12 (Figure S7C) as well as in BR KO "NS" cells (Figure S7D), suggesting that the remodeling toward FAO is downstream of SC-XL formation. Consistent with increased FAO, we found that BR KO cardiac mitochondria had higher levels of respiration fueled by a lipid substrate palmitoyl-carnitine (Figure 6D). Lastly, to ask if the increased FAO extended to the organismal level, we measured the respiratory exchange ratio (RER), which is the ratio between carbon dioxide (CO_2) produced and oxygen (O_2) consumed during respiration in intact organisms. RER is used to estimate the substrate preference of tissues (1 = glucose as fuel; 0.7 = lipids as fuel). Indeed, BR KO mice had significantly lower RER compared with WT mice (Figure 6E). Increased rates of FAO and a reduction in RER occur physiologically during exercise, particularly following prolonged exercise where skeletal muscles switch from utilizing glucose to fatty acids. We therefore hypothesized that BR KO mice—with its remodeling toward a preference for FAO—would perform better under an endurance exercise challenge. Acutely challenged BR KO mice showed a mildly reduced tolerance for forced exercise (Figure 6D) and reduced voluntary exercise activity (Figure 6G). This arises from the lower CIII activity as previously reported.[37] However, upon training—a process associated with remodeling of muscle fibers toward FAO, as evidenced by the lowering of whole body RER in WT animals (Figure S7E)—BR KO mice surprisingly had enhanced performance in the forced exercise test compared with untrained BR KO mice (Figure 6F) and displayed the same levels of voluntary exercise to WT as approximated by energy expenditure (Figure 6G). These data suggest that the metabolic remodeling accompanying an increased in the ratio of SC-XL: free CIII is

(F) Electron micrographs of WT and BR KO cardiac mitochondria at 9 and 18 weeks (left), with cristae architecture quantification (right). Data as mean ± SEM, *n* = 12.

(G) Lipidomic quantification of cardiolipin species in WT and BR KO cardiac mitochondria. CL 72:8 CL(36:4)(36:4) represents mature cardiolipin. Data as mean ± SEM, *n* = 3.

All *p* values are from two-tailed unpaired t test.

Please cite this article in press as: Liang et al., Formation of I_2+III_2 supercomplex rescues respiratory chain defects, Cell Metabolism (2024), https://doi.org/10.1016/j.cmet.2024.11.011

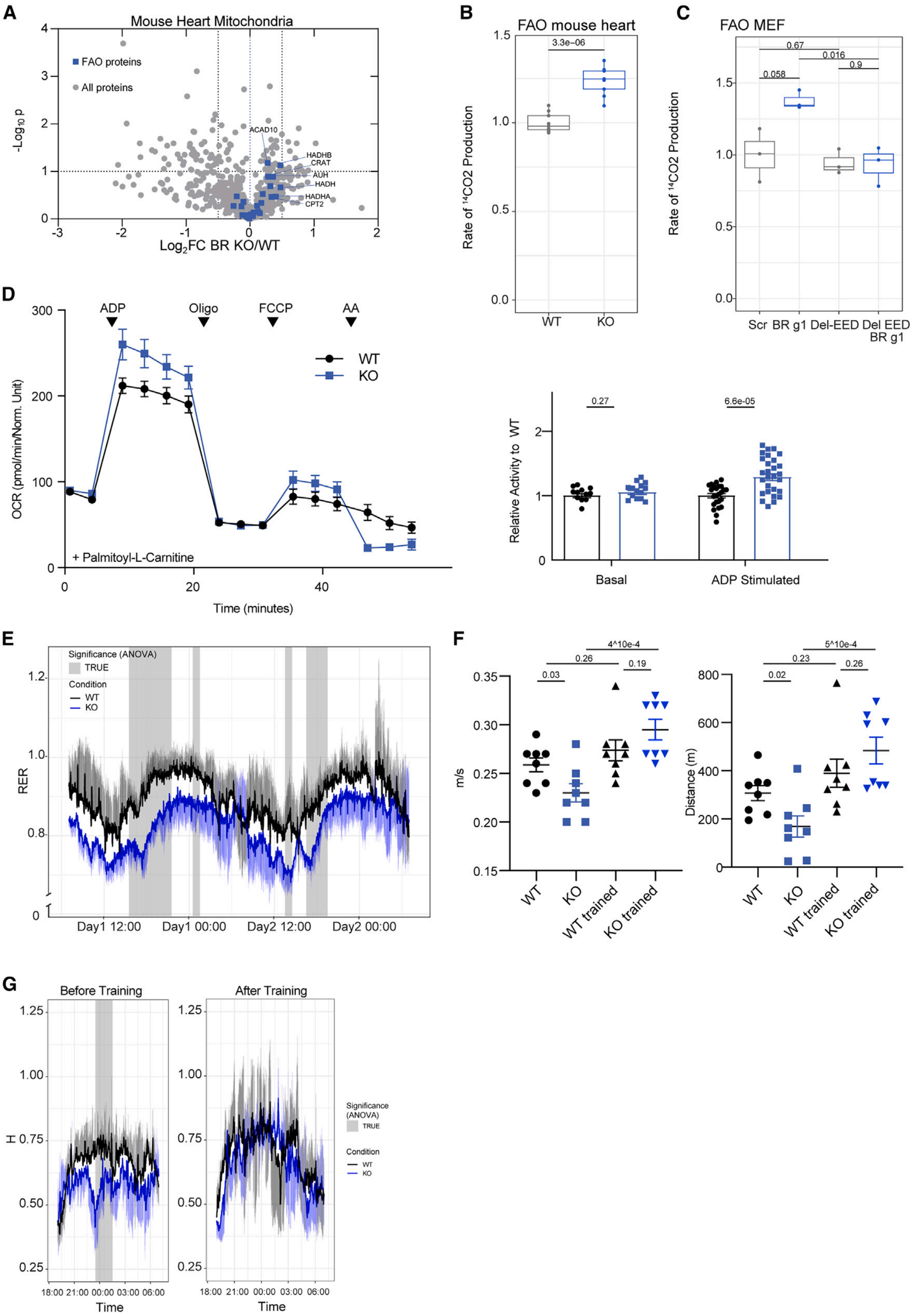

(legend on next page)

Please cite this article in press as: Liang et al., Formation of I_2+III_2 supercomplex rescues respiratory chain defects, Cell Metabolism (2024), https://doi.org/10.1016/j.cmet.2024.11.011

associated with increased preference for FAO, leading to a functionally enhanced performance upon endurance training.

SC-XL is associated with protection against ischemia-reperfusion-induced heart failure

In light of the observed protection against oxidative stress, we hypothesized that SC-XL formation in BR KO mice would offer protection against cardiac diseases caused by a reduction in mitochondrial energy efficiency and increased oxidative stress. Cardiac mitochondria isolated from dogs with heart failure have reduced levels of SCs and OXPHOS.[59] In particular, we postulated that the SC-XL would offer protection against ischemia-reperfusion injury (IRI) and the ensuing heart failure. In the acute phase of cardiac IRI, cardiomyocytes die from ATP depletion, a transient burst of CI ROS from RET,[60] calcium overload, and ultimately the opening of the mitochondrial permeability transition pore (mPTP). Pharmacological blockade of CI RET ROS[61] or the mPTP[62] has cardioprotective effects to reduce infarct size following cardiac IR. In the chronic phase of adverse cardiac remodeling, post-IRI cardiomyocytes suffer from mitochondrial dysfunction and energy starvation, elevated levels of ROS leading to inflammation and fibrosis,[63,64] as well as a maladaptive reprogramming away from FAO and glucose oxidation to glycolytic modes of ATP production.[65] Mitochondria with increased SC-XL would therefore be predicted to be protected against both phases of IRI owing to reduced ROS production, increased bioenergetic efficiency, and mitochondrial integrity as well as a preference for FAO.

To test this hypothesis, we subjected BR KO male mice and WT littermates to a cardiac IRI model with 45 min of ischemia followed by reperfusion and examined cardiac function 4 weeks post-IRI (Figure 7A). Although BR KO and WT mice had indistinguishable cardiac echocardiography parameters in the basal state (Figure S7F), we found that BR KO mice at 4 weeks post-IRI had improved cardiac function as evidenced by better-preserved ejection fraction (EF) and left ventricular end-diastolic and systolic diameters (LVEDd/s), which were compromised following IRI (Figure 7B). Consistent with the improved cardiac function, the infarct size as measured by histological analysis of dead cardiac tissue was significantly reduced in BR KO mice (Figure 7C). Lastly, BR KO hearts had a significantly lower level of cardiac fibrosis as measured by Masson's trichome staining for collagen deposition within the myocardium (Figures 7D and S7G). We then asked if enhanced FAO in BR KO is associated with the observed protection against IRI. In WT mice, FAO was reduced 4 weeks post-IRI, in line with the known switch away to glycolysis in this model of heart failure (Figure 7E). By contrast, the attenuation in FAO was completely blocked in BR KO mice following IRI, suggesting that BR KO cardiac mitochondria were protected from detrimental metabolic reprogramming following IRI. Altogether, these results suggest that SC-XL formation in BR KO mitochondria is correlated with better outcomes following IRI.

DISCUSSION

To maintain homeostasis, mammalian mitochondria display a high degree of plasticity to mild metabolic insults. This intrinsic property of mitochondria to "self-heal" is known as "mitohormesis," a biological process in which exposure to mild stressors, such as ROS, can stimulate beneficial adaptations in cells and improve their overall function. Here, we sought to ask whether respiratory SC formation is a mitohormetic mechanism in response to defects in individual ETC complexes. Unexpectedly, we found that partial reduction in the levels of CIII, but not CI or CIV, is sufficient to induce all remaining CIII to associate with CI in a very specific and large respirasome—called SC-XL. This phenomenon is conserved in humans,[35] mouse (this study), and Drosophila[66] and allows mitochondria with CIII deficiency to maintain normal levels of respiration under normal, unchallenged conditions *in vitro* and *in vivo*. Compromising SC-XL formation leads to decompensation, revealing a respiratory defect caused by the underlying CIII deficiency. Furthermore, SC-XL reduced CIII ROS production and enhanced FAO. Consequently, BR KO mice show greater improvement in endurance exercise following training and are protected from ischemic heart failure driven prominently by RET-driven ROS. Of note, there is still considerable debate at present over the metabolic and physiological effects of contact site mutations that prevent CI and CIII association and SC formation. While Larsson and colleagues found that the Uqcrc1$^{\mathrm{DEL:E258\text{-}D260}}$ had no effects on murine respiration both *in vitro* and *in vivo*,[22] Harper and colleagues found that mutating the cognate contact point of UQCRC1$^{\mathrm{E258\text{-}D260}}$ in CI (NDUFB4$^{\mathrm{N24,\ R30}}$) resulted in lowered respiratory competence in cultured human cells.[67] Here, we found that removing the SC-XL in BR KO cells using the UQCRC1$^{\mathrm{DEL:E258\text{-}D260}}$ mutation resulted in respiratory decompensation. Hence, we believe that while SCs might have cell-type- or context-specific contribution to physiological respiration, their function becomes indispensable when cells are challenged with an ETC perturbation. SC-XL formation may also mask the true burden and incidence of CIII mutations in the human population, especially those in accessorial or peripheral subunits that can be efficiently buffered by SC-XL.

Figure 6. SC-XL increases FAO and trained endurance exercise

(A) Volcano plot of MS analysis of WT and BR KO cardiac mitochondria, with fatty acid oxidation (FAO) proteins highlighted.

(B) FAO analysis via $^{14}CO_2$ release from ^{14}C-palmitic acid in WT and BR KO cardiac homogenates. Data as mean ± SEM, $n = 8$.

(C) FAO analysis via $^{14}CO_2$ release from ^{14}C-palmitic acid in WT or BR KO C2C12 cells. Data as mean ± SEM, $n = 6$.

(D) Oxygen consumption in WT and BR KO cardiac mitochondria with palmitoyl-L-carnitine. Seahorse trace (top) and OCR quantification (bottom). Data as mean ± SEM, $n = 24$; p values from two-tailed unpaired t test.

(E) Respiratory exchange ratio (RER) in WT and BR KO male mice. Significant regions are shaded in gray, defined by $p < 0.05$ by ANCOVA testing.

(F) Exercise capacity of 20-week-old male BR KO mice assessed by forced treadmill running with WT controls. Maximum speed and distance plotted. Data as mean ± SEM, $n = 8$.

(G) Whole-body energy expenditure (H) measured by indirect calorimetry in WT and BR KO mice, before (left) and after (right) exercise training. Significant regions are shaded in gray, defined by $p < 0.05$ by ANCOVA testing.

All p values are from two-tailed unpaired t test, unless otherwise stated.

Please cite this article in press as: Liang et al., Formation of I_2+III_2 supercomplex rescues respiratory chain defects, Cell Metabolism (2024), https://doi.org/10.1016/j.cmet.2024.11.011

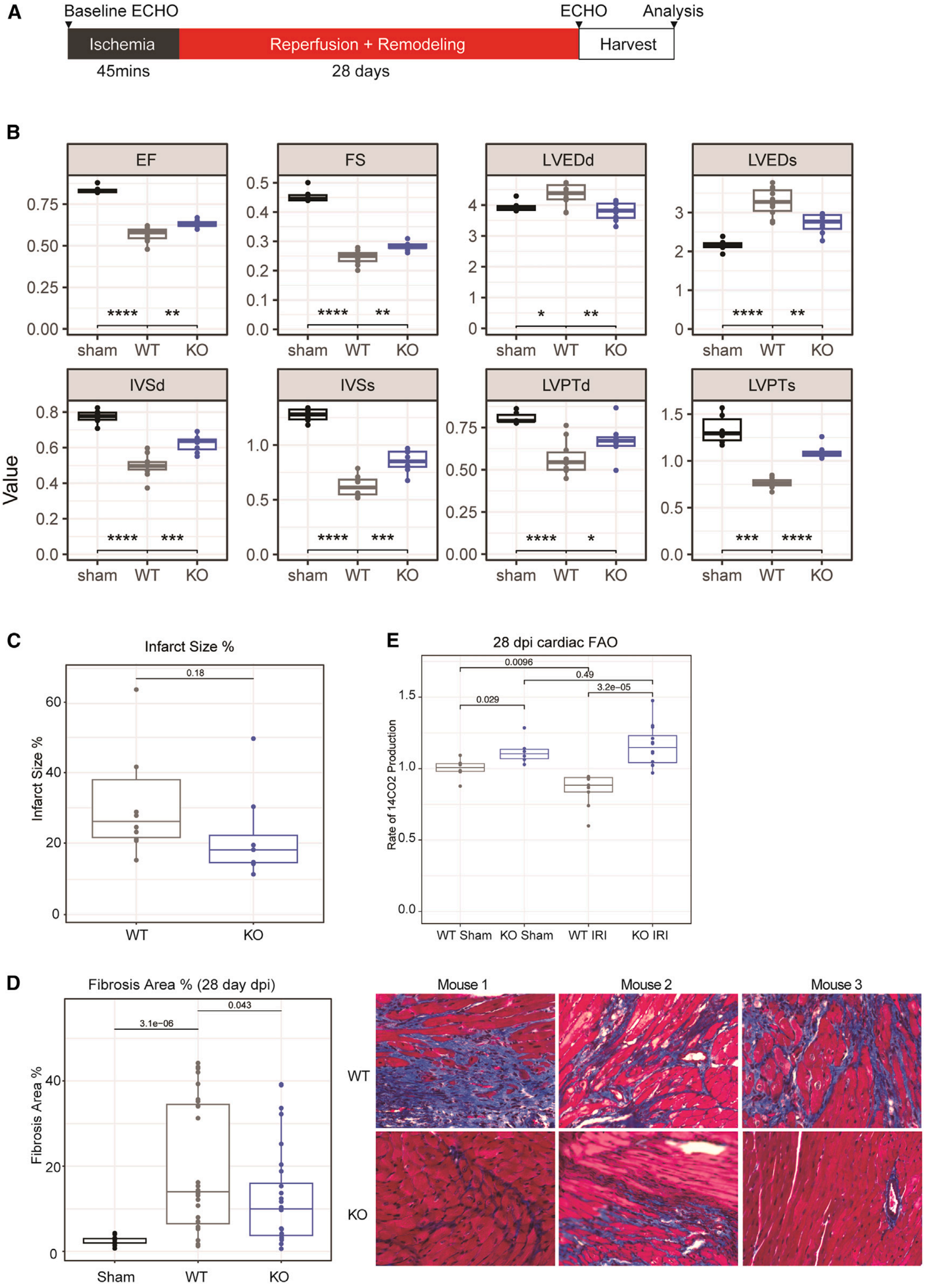

Figure 7. SC-XL formation is associated with cardioprotection

(A) Schematic of ischemic reperfusion injury (IRI) model.

(B) Cardiac parameters by echocardiography of sham, WT, and BR KO mice 4 weeks post-IRI (EF, ejection fraction; FS, fraction shortening; IVSd/IVSs, interventricular septum thickness at diastole/systole; LVEDD/LVESd, left ventricular end-diastolic/systolic diameter; LVPTd/LVPTs, left ventricular posterior wall thickness at diastole/systole). Data as mean ± SEM, *n* = 6 (sham), 8 (WT), 7 (BR KO).

(C) Left ventricular infarct size in WT and BR KO mice 4 weeks post-IRI. Data as mean ± SEM, *n* = 8 (WT), 7 (BR KO).

(legend continued on next page)

Please cite this article in press as: Liang et al., Formation of I_2+III_2 supercomplex rescues respiratory chain defects, Cell Metabolism (2024), https://doi.org/10.1016/j.cmet.2024.11.011

The structure of the SC-XL—at present resolution—shows no major differences in the interfaces or composition of CI and CIII from that of known CI+CIII-containing SCs. This demonstrates that neither addition nor removal of canonical subunits is required to form the SC-XL. Rather, the driving force for SC-XL formation appears to be the preferred association between nascent CIII and CI during assembly, under conditions when the ratio of CI:CIII is increased (i.e., CIII deficiency). In this case, residual CIII becomes “saturated” with CI, possibly as a strategy for enhanced stabilization.[66] SC-XL formation might also be enabled by a slow-down in CIII assembly due to defects in both assembly factors, such as BR. This could cause a buildup of a particular CIII assembly intermediate, favoring their interaction with cognate CI assembly intermediates that promote SC-XL formation. How elevated $CoQH_2$/CoQ ratio contributes to this process is unclear but could involve a feedback mechanism to alter the dynamics of CI or CIII assembly to favor SC-XL formation.

We show here that SC-XL maximizes CIII activity and minimizes ROS production, making it well suited to compensate for reduced CIII activity. In line with our observation that there is similar cryo-EM density for the two Riske FeS head domains in the III_2 dimer of the SC-XL, a tantalizing hypothesis is that the two CIs arranged around a central III_2 dimer restore the functional symmetry of the CIII dimer. This would increase CIII activity per unit of CIII enzyme and could represent a “CIII-saving” mechanism. Why the SC-XL would not be the default arrangement of ETC is unclear. One possibility is that the depletion of CIV from the SC-XL still puts it at a disadvantage compared with bona fide respirasomes, resulting in the observed lower exercise tolerance in the basal untrained state. Thus, although SC-XL is protective against ROS and ischemia, the SC I+III_2+IV respirasomes might still be the most efficient mode of ETC arrangement under normal conditions to allow for directed electron flow between CI and CIV.[13]

Altogether, our study demonstrates that SC formation is dynamic and responsive to physiologically relevant metabolic stressors, including intrinsic mitochondrial perturbations. SC-XL formation is necessary and sufficient to compensate for CIII deficiency *in vivo* and does so by enabling a highly efficient, “CIII-saving” mode of OXPHOS. Furthermore, this is the first demonstration that increased formation of a respiratory SC can protect against a ROS-driven pathology such as cardiac IRI—lending credence to the long-held but poorly substantiated claims that SCs can reduce pathologic ROS generation by the ETC. This should stimulate efforts to induce the formation of SCs *in vivo* for therapeutic benefit in diseases characterized by mitochondrial decline and dysfunction.

Limitations of the study

A major limitation of our paper is the inability to pinpoint the molecular mechanism required for SC-XL formation, as mentioned above. We are also unable to identify an assembly intermediate that points to increased association between CI and CIII as such an intermediate may be too transient to be captured by complexome profiling. Therefore, the exact proteins, intermediates, signaling pathways, and transcriptional programs required for SC-XL formation warrant further investigation. Our structural analysis requires further work to attain atomic resolution, which will hopefully reveal how SC-XL formation increases the efficiency of CIII and reduces ROS emission from the Qo site. Data derived from “NS” cells presented in this study—even though they agree with data derived from the UQCRC1$^{DEL-EED}$ system—should be interpreted with caution, since the underlying mutation that leads to the loss of SC-XL is unknown. Additionally, we cannot uncouple the contribution of the SC-XL to cardioprotection from that of having reduced CIII and CIV activity, which might also be beneficial in ischemic settings. It is possible that it is the combination of increased SC-XL and reduced free complexes rather than increased SC-XL alone that provides optimal benefit to the animals. The mechanisms of the SC-XL in cardioprotection—reduced CIII ROS and CI RET ROS and enhanced FAO—is also speculative at present and may be indirect, warranting further investigation. Lastly, our model predicts that introducing the UQCRC1$^{DEL-EED}$ mutation into the BR KO mouse will result in whole-body decompensation, even though this was only demonstrated at the cellular level. This remains to be seen and should be the subject of future investigation.

RESOURCE AVAILABILITY

Lead contact

Further information and requests for resources and reagents should be directed to and will be fulfilled by the lead contact, Lena Ho (lena@ho-lab.org).

Materials availability

Unique reagents generated in this study will be made available upon reasonable request to the lead contact with a completed Materials Transfer Agreement.

Data and code availability

For previously published BR KO mouse data[37] see accession database PXD030258. C2C12 data can be found ProteomeXchange Consortium via the PRIDE partner repository with the dataset identifier PXD044761. Complexome profiling data can be found ProteomeXchange Consortium via the PRIDE partner repository with the database PXD044957. All reagents cited, including animals, will be available upon request through MTA. Raw cryo-EM micrographs used in this study, composite map, focused refinements, and model for *M. musculus* SC-XL will be made available on the Electron Microscopy Public Image Archive (EMPIAR) database, the Electron Microscopy Database (EMDB) and the Protein Data Bank (PDB). Unprocessed data underlying the display items in the manuscript, related to Figures 1, 2, 3, 4, 5, 6, 7, and S1–S7, are compiled as Data S1.zip. No new code has been generated in this study. Any additional information required to reanalyze the data reported in this paper is available from the lead contact upon request.

ACKNOWLEDGMENTS

We thank Nils-Göran Larsson (Karolinska Institute) for the kind gift of the Uqcrc1$^{DEL-EED}$ MEFs; Sun Lei (Duke-NUS) for the kind gift of the BR KO mouse;

(D) Left ventricular fibrosis area in WT and BR KO mice 4 weeks post-IRI. Data as mean ± SEM, *n* = 6 (sham), 8 (WT), 7 (BR KO). Masson’s trichrome images on the right.

(E) FAO measured by $^{14}CO_2$ release from ^{14}C-palmitic acid in cardiac homogenates 4 weeks post-IRI. Data as mean ± SEM, *n* = 6 (WT sham), 6 (KO sham), 8 (WT IRI), and 7 (BR KO IRI).

All *p* values are from two-tailed unpaired t test.

Peh Jih Hou, Marianne DeRoose, and Cardiolab LLC (Maryland, USA) for technical assistance with mouse experiments and cardiac IRI phenotyping; Charlene Chan for assistance with mass spectrometry; the Duke-NUS Metabolomics core facility for metabolomics analyses; the Bio21 Mass Spectrometry and Proteomics Facility (MMSPF) for the provision of instrumentation, training, and technical support; and Navdeep Chandel lab (Northwestern) for the pLV-EF1-AOX construct. This work was supported by MOH-000960, MOH-001394, and H23G2A0061 awarded to L.H. and Duke/Duke-NUS/RECA(Pilot)/2019/0045 awarded to L.H. and D.M. D.K. is supported by the National Research Foundation Singapore and the Singapore Ministry of Education under its Research Centres of Excellence initiative. D.A.S. is supported by GNT1140906 and GNT2009732 from the National Health & Medical Research Council. A.P. and J.A.L. are funded by the NIGMS of the NIH under award R35GM137929. C.U. is supported by Ministerio de Ciencia, Innovación y Universidades, Spain (PID2023-147288NB-I00) and by the Caixa Research Health program (HR24-00604). The content is solely the responsibility of the authors and does not necessarily represent the official views of the National Institutes of Health.

AUTHOR CONTRIBUTIONS

L.H., C.L., A.P., S.Z., and J.A.L. conceived and designed the experiments in the paper. L.H., C.L., S.Z., S.B., D.R.L.R., T.R.K., J.M., A.P., A.C.-O., J.A.L., Y.-J.W., H.O., C.W., M.W., R.L., J.M.J., S.R., and M.I. performed the experiments and collected and analyzed the data. D.K., K.F., D.M., C.U., I.W., and D.A.S. contributed ideas and data analysis. A.M.G. and C.U. provided key cell lines. L.H., J.A.L., and C.L. wrote the paper.

DECLARATION OF INTERESTS

The authors declare no competing interests.

STAR★METHODS

Detailed methods are provided in the online version of this paper and include the following:

- KEY RESOURCES TABLE
- METHOD DETAILS
    - ○ Animals
    - ○ Indirect Calorimetry by Phenomaster
    - ○ Mouse treadmill exercise
    - ○ Cell lines
    - ○ Cell culture
    - ○ Doxycycline Pulse Chase
    - ○ AAV production and infection
    - ○ Mitochondria isolation
    - ○ Cardiolipin Quantification
    - ○ C2C12 mitochondrial proteome analysis
    - ○ Complexome Profiling
    - ○ Stoichiometry Determination
    - ○ SDS-PAGE and immunoblotting
    - ○ Native PAGE
    - ○ Respiratory activity of excised gel slices
    - ○ Gene editing by CRISPR
    - ○ Virus production and transduction
    - ○ Seahorse assay
    - ○ Isolated Mitochondria Seahorse and Electron Flow
    - ○ Citrate synthase activity assay
    - ○ Electron transport chain complex purification
    - ○ CryoEM grid preparation and data collection
    - ○ CryoEM image processing
    - ○ Model building and refinement
    - ○ Sucrose gradient fractionation
    - ○ Respiratory complex activity
    - ○ Site Specific Respiratory ROS quantification
    - ○ ^{14}C 1-Palmitic acid coupled fatty acid oxidation assay (FAO)
    - ○ Ischemic Reperfusion Injury mouse model
    - ○ Mitochondrial Respirometric Phenotyping
    - ○ Quantitative PCR Assay
    - ○ mtDNA quantification
    - ○ CoQ Measurement
    - ○ Mouse Body Composition Measurement
    - ○ Statistical Analysis

SUPPLEMENTAL INFORMATION

Supplemental information can be found online at https://doi.org/10.1016/j.cmet.2024.11.011.

Received: September 11, 2023
Revised: July 29, 2024
Accepted: November 14, 2024
Published: January 8, 2025

REFERENCES

1. Lenaz, G., Tioli, G., Falasca, A.I., and Genova, M.L. (2016). Complex I function in mitochondrial supercomplexes. Biochim. Biophys. Acta *1857*, 991–1000. https://doi.org/10.1016/j.bbabio.2016.01.013.
2. Letts, J.A., Fiedorczuk, K., Degliesposti, G., Skehel, M., and Sazanov, L.A. (2019). Structures of respiratory supercomplex I+III2 reveal functional and conformational crosstalk. Mol. Cell *75*, 1131–1146.e6. https://doi.org/10.1016/j.molcel.2019.07.022.
3. Vercellino, I., and Sazanov, L.A. (2021). Structure and assembly of the mammalian mitochondrial supercomplex CIII2CIV. Nature *598*, 364–367. https://doi.org/10.1038/s41586-021-03927-z.
4. Letts, J.A., Fiedorczuk, K., and Sazanov, L.A. (2017). The architecture of respiratory supercomplexes. Biophys. J. *112*, 278a. https://doi.org/10.1016/j.bpj.2016.11.1504.
5. Sousa, J.S., Mills, D.J., Vonck, J., and Kühlbrandt, W. (2016). Functional asymmetry and electron flow in the bovine respirasome. eLife *5*, e21290. https://doi.org/10.7554/eLife.21290.
6. Guo, R., Zong, S., Wu, M., Gu, J., and Yang, M. (2017). Architecture of human mitochondrial respiratory megacomplex I2III2IV2. Cell *170*, 1247–1257.e12. https://doi.org/10.1016/j.cell.2017.07.050.
7. Mühleip, A., Flygaard, R.K., Baradaran, R., Haapanen, O., Gruhl, T., Tobiasson, V., Maréchal, A., Sharma, V., and Amunts, A. (2023). Structural basis of mitochondrial membrane bending by the I–II–III2–IV2 supercomplex. Nature *615*, 934–938. https://doi.org/10.1038/s41586-023-05817-y.
8. Maranzana, E., Barbero, G., Falasca, A.I., Lenaz, G., and Genova, M.L. (2013). Mitochondrial respiratory supercomplex association limits production of reactive oxygen species from Complex I. Antioxid. Redox Signal. *19*, 1469–1480. https://doi.org/10.1089/ars.2012.4845.
9. Acín-Pérez, R., Bayona-Bafaluy, M.P., Fernández-Silva, P., Moreno-Loshuertos, R., Pérez-Martos, A., Bruno, C., Moraes, C.T., and Enríquez, J.A. (2004). Respiratory Complex III is required to maintain complex I in mammalian mitochondria. Mol. Cell *13*, 805–815. https://doi.org/10.1016/s1097-2765(04)00124-8.
10. Diaz, F., Fukui, H., Garcia, S., and Moraes, C.T. (2006). Cytochrome c oxidase is required for the assembly/stability of respiratory complex I in mouse fibroblasts. Mol. Cell. Biol. *26*, 4872–4881. https://doi.org/10.1128/MCB.01767-05.
11. Berndtsson, J., Kohler, A., Rathore, S., Marin-Buera, L., Dawitz, H., Diessl, J., Kohler, V., Barrientos, A., Büttner, S., Fontanesi, F., et al. (2020). Respiratory supercomplexes enhance electron transport by decreasing cytochrome c diffusion distance. EMBO Rep. *21*, e51015. https://doi.org/10.15252/embr.202051015.
12. Lapuente-Brun, E., Moreno-Loshuertos, R., Acín-Pérez, R., Latorre-Pellicer, A., Colás, C., Balsa, E., Perales-Clemente, E., Quirós, P.M., Calvo, E., Rodríguez-Hernández, M.A., et al. (2013). Supercomplex assembly determines electron flux in the mitochondrial electron transport chain. Science *340*, 1567–1570. https://doi.org/10.1126/science.1230381.

Please cite this article in press as: Liang et al., Formation of I_2+III_2 supercomplex rescues respiratory chain defects, Cell Metabolism (2024), https://doi.org/10.1016/j.cmet.2024.11.011

13. Lenaz, G., and Genova, M.L. (2009). Mobility and function of coenzyme Q (ubiquinone) in the mitochondrial respiratory chain. Biochim. Biophys. Acta *1787*, 563–573. https://doi.org/10.1016/j.bbabio.2009.02.019.
14. Bianchi, C., Genova, M.L., Parenti Castelli, G.P., and Lenaz, G. (2004). The mitochondrial respiratory chain is partially organized in a supercomplex assembly KINETIC EVIDENCE USING FLUX CONTROL ANALYSIS*. J. Biol. Chem. *279*, 36562–36569. https://doi.org/10.1074/jbc.M405135200.
15. Blaza, J.N., Serreli, R., Jones, A.J.Y., Mohammed, K., and Hirst, J. (2014). Kinetic evidence against partitioning of the ubiquinone pool and the catalytic relevance of respiratory-chain supercomplexes. Proc. Natl. Acad. Sci. USA *111*, 15735–15740. https://doi.org/10.1073/pnas.1413855111.
16. Fedor, J.G., and Hirst, J. (2018). Mitochondrial supercomplexes do not enhance catalysis by quinone channeling. Cell Metab. *28*, 525–531.e4. https://doi.org/10.1016/j.cmet.2018.05.024.
17. Ikeda, K., Shiba, S., Horie-Inoue, K., Shimokata, K., and Inoue, S. (2013). A stabilizing factor for mitochondrial respiratory supercomplex assembly regulates energy metabolism in muscle. Nat. Commun. *4*, 2147. https://doi.org/10.1038/ncomms3147.
18. Balsa, E., Soustek, M.S., Thomas, A., Cogliati, S., García-Poyatos, C., Martín-García, E., Jedrychowski, M., Gygi, S.P., Enriquez, J.A., and Puigserver, P. (2019). ER and nutrient stress promote assembly of respiratory chain supercomplexes through the PERK-eIF2α axis. Mol. Cell *74*, 877–890.e6. https://doi.org/10.1016/j.molcel.2019.03.031.
19. Garaude, J., Acín-Pérez, R., Martínez-Cano, S., Enamorado, M., Ugolini, M., Nistal-Villán, E., Hervás-Stubbs, S., Pelegrín, P., Sander, L.E., Enríquez, J.A., et al. (2016). Mitochondrial respiratory-chain adaptations in macrophages contribute to antibacterial host defense. Nat. Immunol. *17*, 1037–1045. https://doi.org/10.1038/ni.3509.
20. Calvo, E., Cogliati, S., Hernansanz-Agustín, P., Loureiro-López, M., Guarás, A., Casuso, R.A., García-Marqués, F., Acín-Pérez, R., Martí-Mateos, Y., Silla-Castro, J.C., et al. (2020). Functional role of respiratory supercomplexes in mice: SCAF1 relevance and segmentation of the Qpool. Sci. Adv. *6*, eaba7509. https://doi.org/10.1126/sciadv.aba7509.
21. Fernández-Vizarra, E., López-Calcerrada, S., Formosa, L.E., Pérez-Pérez, R., Ding, S., Fearnley, I.M., Arenas, J., Martín, M.A., Zeviani, M., Ryan, M.T., et al. (2021). SILAC-based complexome profiling dissects the structural organization of the human respiratory supercomplexes in SCAFIKO cells. Biochim. Biophys. Acta Bioenerg. *1862*, 148414. https://doi.org/10.1016/j.bbabio.2021.148414.
22. Milenkovic, D., Misic, J., Hevler, J.F., Molinié, T., Chung, I., Atanassov, I., Li, X., Filograna, R., Mesaros, A., Mourier, A., et al. (2023). Preserved respiratory chain capacity and physiology in mice with profoundly reduced levels of mitochondrial respirasomes. Cell Metab. *35*, 1799–1813.e7. https://doi.org/10.1016/j.cmet.2023.07.015.
23. Vercellino, I., and Sazanov, L.A. (2021). The assembly, regulation and function of the mitochondrial respiratory chain. Nat. Rev. Mol. Cell Biol. *23*, 141–161. https://doi.org/10.1038/s41580-021-00415-0.
24. Bennett, C.F., Latorre-Muro, P., and Puigserver, P. (2022). Mechanisms of mitochondrial respiratory adaptation. Nat. Rev. Mol. Cell Biol. *23*, 817–835. https://doi.org/10.1038/s41580-022-00506-6.
25. Bennett, C.F., O'Malley, K.E., Perry, E.A., Balsa, E., Latorre-Muro, P., Riley, C.L., Luo, C., Jedrychowski, M., Gygi, S.P., and Puigserver, P. (2021). Peroxisomal-derived ether phospholipids link nucleotides to respirasome assembly. Nat. Chem. Biol. *17*, 703–710. https://doi.org/10.1038/s41589-021-00772-z.
26. Kobayashi, A., Azuma, K., Takeiwa, T., Kitami, T., Horie, K., Ikeda, K., and Inoue, S. (2023). A FRET-based respirasome assembly screen identifies spleen tyrosine kinase as a target to improve muscle mitochondrial respiration and exercise performance in mice. Nat. Commun. *14*, 312. https://doi.org/10.1038/s41467-023-35865-x.
27. Fernández-Vizarra, E., López-Calcerrada, S., Sierra-Magro, A., Pérez-Pérez, R., Formosa, L.E., Hock, D.H., Illescas, M., Peñas, A., Brischigliaro, M., Ding, S., et al. (2022). Two independent respiratory chains adapt OXPHOS performance to glycolytic switch. Cell Metab. *34*, 1792–1808.e6. https://doi.org/10.1016/j.cmet.2022.09.005.
28. Brischigliaro, M., Cabrera-Orefice, A., Arnold, S., Viscomi, C., Zeviani, M., and Fernández-Vizarra, E. (2023). Structural rather than catalytic role for mitochondrial respiratory chain supercomplexes. eLife *12*, RP88084. https://doi.org/10.7554/eLife.88084.
29. To, T.-L., Cuadros, A.M., Shah, H., Hung, W.H.W., Li, Y., Kim, S.H., Rubin, D.H.F., Boe, R.H., Rath, S., Eaton, J.K., et al. (2019). A compendium of genetic modifiers of mitochondrial dysfunction reveals intra-organelle buffering. Cell *179*, 1222–1238.e17. https://doi.org/10.1016/j.cell.2019.10.032.
30. Calvo, S.E., Tucker, E.J., Compton, A.G., Kirby, D.M., Crawford, G., Burtt, N.P., Rivas, M., Guiducci, C., Bruno, D.L., Goldberger, O.A., et al. (2010). High-throughput, pooled sequencing identifies mutations in NUBPL and FOXRED1 in human complex I deficiency. Nat. Genet. *42*, 851–858. https://doi.org/10.1038/ng.659.
31. Pagliarini, D.J., Calvo, S.E., Chang, B., Sheth, S.A., Vafai, S.B., Ong, S.-E., Walford, G.A., Sugiana, C., Boneh, A., Chen, W.K., et al. (2008). A mitochondrial protein compendium elucidates Complex I disease biology. Cell *134*, 112–123. https://doi.org/10.1016/j.cell.2008.06.016.
32. Zhang, S., Reljić, B., Liang, C., Kerouanton, B., Francisco, J.C., Peh, J.H., Mary, C., Jagannathan, N.S., Olexiouk, V., Tang, C., et al. (2020). Mitochondrial peptide BRAWNIN is essential for vertebrate respiratory complex III assembly. Nat. Commun. *11*, 1312. https://doi.org/10.1038/s41467-020-14999-2.
33. Hell, K., Tzagoloff, A., Neupert, W., and Stuart, R.A. (2000). Identification of Cox20p, a novel protein involved in the maturation and assembly of cytochrome oxidase Subunit 2. J. Biol. Chem. *275*, 4571–4578. https://doi.org/10.1074/jbc.275.7.4571.
34. Tropeano, C.V., Aleo, S.J., Zanna, C., Roberti, M., Scandiffio, L., Polosa, P.L., Fiori, J., Porru, E., Roda, A., Carelli, V., et al. (2020). Fine-tuning of the respiratory complexes stability and supercomplexes assembly in cells defective of complex III. Biochim. Biophys. Acta Bioenerg. *1861*, 148133. https://doi.org/10.1016/j.bbabio.2019.148133.
35. Vidali, S., Gerlini, R., Thompson, K., Urquhart, J.E., Meisterknecht, J., Aguilar-Pimentel, J.A., Amarie, O.V., Becker, L., Breen, C., Calzada-Wack, J., et al. (2021). Characterising a homozygous two-exon deletion in UQCRH: comparing human and mouse phenotypes. EMBO Mol. Med. *13*, e14397. https://doi.org/10.15252/emmm.202114397.
36. Protasoni, M., Pérez-Pérez, R., Lobo-Jarne, T., Harbour, M.E., Ding, S., Peñas, A., Diaz, F., Moraes, C.T., Fearnley, I.M., Zeviani, M., et al. (2020). Respiratory supercomplexes act as a platform for complex III -mediated maturation of human mitochondrial complexes I and IV. EMBO J. *39*, e102817. https://doi.org/10.15252/embj.2019102817.
37. Liang, C., Zhang, S., Robinson, D., Ploeg, M.V., Wilson, R., Nah, J., Taylor, D., Beh, S., Lim, R., Sun, L., et al. (2022). Mitochondrial microproteins link metabolic cues to respiratory chain biogenesis. Cell Rep. *40*, 111204. https://doi.org/10.1016/j.celrep.2022.111204.
38. Greggio, C., Jha, P., Kulkarni, S.S., Lagarrigue, S., Broskey, N.T., Boutant, M., Wang, X., Conde Alonso, S.C., Ofori, E., Auwerx, J., et al. (2017). Enhanced respiratory chain supercomplex formation in response to exercise in human skeletal muscle. Cell Metab. *25*, 301–311. https://doi.org/10.1016/j.cmet.2016.11.004.
39. Sin, J., Andres, A.M., Taylor, D.J.R., Weston, T., Hiraumi, Y., Stotland, A., Kim, B.J., Huang, C., Doran, K.S., and Gottlieb, R.A. (2016). Mitophagy is required for mitochondrial biogenesis and myogenic differentiation of C2C12 myoblasts. Autophagy *12*, 369–380. https://doi.org/10.1080/15548627.2015.1115172.
40. Fisher-Wellman, K.H., Davidson, M.T., Narowski, T.M., Lin, C.-T., Koves, T.R., and Muoio, D.M. (2018). Mitochondrial diagnostics: A multiplexed assay platform for comprehensive assessment of mitochondrial energy fluxes. Cell Rep. *24*, 3593–3606.e10. https://doi.org/10.1016/j.celrep.2018.08.091.
41. Hernansanz-Agustín, P., and Enríquez, J.A. (2021). Generation of reactive oxygen species by mitochondria. Antioxidants (Basel) *10*, 415. https://doi.org/10.3390/antiox10030415.

42. Giese, H., Meisterknecht, J., Heidler, J., and Wittig, I. (2021). Mitochondrial complexome profiling. Methods Mol. Biol. *2192*, 269–285. https://doi.org/10.1007/978-1-0716-0834-0_19.

43. Agip, A.A., Blaza, J.N., Bridges, H.R., Viscomi, C., Rawson, S., Muench, S.P., and Hirst, J. (2018). Cryo-EM structures of complex I from mouse heart mitochondria in two biochemically defined states. Nat. Struct. Mol. Biol. *25*, 548–556. https://doi.org/10.1038/s41594-018-0073-1.

44. Grba, D.N., Chung, I., Bridges, H.R., Agip, A.A., and Hirst, J. (2023). Investigation of hydrated channels and proton pathways in a high-resolution cryo-EM structure of mammalian complex I. Sci. Adv. *9*, eadi1359. https://doi.org/10.1126/sciadv.adi1359.

45. Letts, J.A., and Sazanov, L.A. (2017). Clarifying the supercomplex: the higher-order organization of the mitochondrial electron transport chain. Nat. Struct. Mol. Biol. *24*, 800–808. https://doi.org/10.1038/nsmb.3460.

46. Letts, J.A., Fiedorczuk, K., and Sazanov, L.A. (2016). The architecture of respiratory supercomplexes. Nature *537*, 644–648. https://doi.org/10.1038/nature19774.

47. Esser, L., Gong, X., Yang, S., Yu, L., Yu, C.-A., and Xia, D. (2006). Surface-modulated motion switch: capture and release of iron–sulfur protein in the cytochrome BC1 complex. Proc. Natl. Acad. Sci. USA *103*, 13045–13050. https://doi.org/10.1073/pnas.0601149103.

48. Guarás, A., Perales-Clemente, E., Calvo, E., Acín-Pérez, R., Loureiro-Lopez, M., Pujol, C., Martínez-Carrascoso, I., Nuñez, E., García-Marqués, F., Rodríguez-Hernández, M.A., et al. (2016). The CoQH2/CoQ ratio serves as a sensor of respiratory chain efficiency. Cell Rep. *15*, 197–209. https://doi.org/10.1016/j.celrep.2016.03.009.

49. Fernandez-Ayala, D.J.M., Sanz, A., Vartiainen, S., Kemppainen, K.K., Babusiak, M., Mustalahti, E., Costa, R., Tuomela, T., Zeviani, M., Chung, J., et al. (2009). Expression of the Ciona intestinalis Alternative Oxidase (AOX) in Drosophila Complements Defects in mitochondrial Oxidative Phosphorylation. Cell Metab. *9*, 449–460. https://doi.org/10.1016/j.cmet.2009.03.004.

50. Lopez-Fabuel, I., Le Douce, J.L., Logan, A., James, A.M., Bonvento, G., Murphy, M.P., Almeida, A., and Bolaños, J.P. (2016). Complex I assembly into supercomplexes determines differential mitochondrial ROS production in neurons and astrocytes. Proc. Natl. Acad. Sci. USA *113*, 13063–13068. https://doi.org/10.1073/pnas.1613701113.

51. Bleier, L., Wittig, I., Heide, H., Steger, M., Brandt, U., and Dröse, S. (2015). Generator-specific targets of mitochondrial reactive oxygen species. Free Radic. Biol. Med. *78*, 1–10. https://doi.org/10.1016/j.freeradbiomed.2014.10.511.

52. Quinlan, C.L., Perevoshchikova, I.V., Hey-Mogensen, M., Orr, A.L., and Brand, M.D. (2013). Sites of reactive oxygen species generation by mitochondria oxidizing different substrates☆. Redox Biol. *1*, 304–312. https://doi.org/10.1016/j.redox.2013.04.005.

53. Dröse, S., and Brandt, U. (2008). The mechanism of mitochondrial superoxide production by the cytochrome BC1 complex. J. Biol. Chem. *283*, 21649–21654. https://doi.org/10.1074/jbc.M803236200.

54. Wong, H.-S., Monternier, P.-A., and Brand, M.D. (2019). S1QELs suppress mitochondrial superoxide/hydrogen peroxide production from site IQ without inhibiting reverse electron flow through Complex I. Free Radic. Biol. Med. *143*, 545–559. https://doi.org/10.1016/j.freeradbiomed.2019.09.006.

55. Chance, B., and Hollunger, G. (1961). The interaction of energy and electron transfer reactions in mitochondria. I. General properties and nature of the products of succinate-linked reduction of pyridine nucleotide. J. Biol. Chem. *236*, 1534–1543.

56. Pfeiffer, K., Gohil, V., Stuart, R.A., Hunte, C., Brandt, U., Greenberg, M.L., and Schägger, H. (2003). Cardiolipin stabilizes respiratory chain supercomplexes. J. Biol. Chem. *278*, 52873–52880. https://doi.org/10.1074/jbc.M308366200.

57. Orr, A.L., Vargas, L., Turk, C.N., Baaten, J.E., Matzen, J.T., Dardov, V.J., Attle, S.J., Li, J., Quackenbush, D.C., Goncalves, R.L.S., et al. (2015). Suppressors of superoxide production from mitochondrial complex III. Nat. Chem. Biol. *11*, 834–836. https://doi.org/10.1038/nchembio.1910.

58. Hirschey, M.D., and Verdin, E. (2010). Measuring fatty acid oxidation in tissue homogenates. Protoc. Exch. https://doi.org/10.1038/nprot.2010.92.

59. Rosca, M.G., Vazquez, E.J., Kerner, J., Parland, W., Chandler, M.P., Stanley, W., Sabbah, H.N., and Hoppel, C.L. (2008). Cardiac mitochondria in heart failure: decrease in respirasomes and oxidative phosphorylation. Cardiovasc. Res. *80*, 30–39. https://doi.org/10.1093/cvr/cvn184.

60. Chouchani, E.T., Pell, V.R., Gaude, E., Aksentijević, D., Sundier, S.Y., Robb, E.L., Logan, A., Nadtochiy, S.M., Ord, E.N.J., Smith, A.C., et al. (2014). Ischaemic accumulation of succinate controls reperfusion injury through mitochondrial ROS. Nature *515*, 431–435. https://doi.org/10.1038/nature13909.

61. Brand, M.D., Goncalves, R.L.S., Orr, A.L., Vargas, L., Gerencser, A.A., Borch Jensen, M., Wang, Y.T., Melov, S., Turk, C.N., Matzen, J.T., et al. (2016). Suppressors of superoxide-H2O2 production at site IQ of mitochondrial Complex I protect against stem cell hyperplasia and ischemia-reperfusion injury. Cell Metab. *24*, 582–592. https://doi.org/10.1016/j.cmet.2016.08.012.

62. Piot, C., Croisille, P., Staat, P., Thibault, H., Rioufol, G., Mewton, N., Elbelghiti, R., Cung, T.T., Bonnefoy, E., Angoulvant, D., et al. (2008). Effect of cyclosporine on reperfusion injury in acute myocardial infarction. N. Engl. J. Med. *359*, 473–481. https://doi.org/10.1056/NEJMoa071142.

63. González, A., Richards, A.M., de Boer, R.A., Thum, T., Arfsten, H., Hülsmann, M., Falcao-Pires, I., Díez, J., Foo, R.S.Y., Chan, M.Y., et al. (2022). Cardiac remodelling – Part 1: From cells and tissues to circulating biomarkers. A review from the Study Group on Biomarkers of the Heart Failure Association of the European Society of Cardiology. Eur. J. Heart Fail. *24*, 927–943. https://doi.org/10.1002/ejhf.2493.

64. Aimo, A., Vergaro, G., González, A., Barison, A., Lupón, J., Delgado, V., Richards, A.M., de Boer, R.A., Thum, T., Arfsten, H., et al. (2022). Cardiac remodelling – Part 2: Clinical, imaging and laboratory findings. A review from the Study Group on Biomarkers of the Heart Failure Association of the European Society of Cardiology. Eur. J. Heart Fail. *24*, 944–958. https://doi.org/10.1002/ejhf.2522.

65. Lopaschuk, G.D., Karwi, Q.G., Tian, R., Wende, A.R., and Abel, E.D. (2021). Cardiac energy metabolism in heart failure. Circ. Res. *128*, 1487–1513. https://doi.org/10.1161/CIRCRESAHA.121.318241.

66. Brischigliaro, M., Cabrera-Orefice, A., Arnold, S., Viscomi, C., Zeviani, M., and Fernández-Vizarra, E. (2023). Structural rather than catalytic role for mitochondrial respiratory chain supercomplexes. Preprint at bioRxiv. https://doi.org/10.1101/2023.04.19.537447.

67. Parmar, G., Fong-McMaster, C., Pileggi, C.A., Patten, D.A., Cuillerier, A., Myers, S., Wang, Y., Hekimi, S., Cuperlovic-Culf, M., and Harper, M.-E. (2024). Accessory subunit NDUFB4 participates in mitochondrial complex I supercomplex formation. J. Biol. Chem. *300*, 105626. https://doi.org/10.1016/j.jbc.2024.105626.

68. Schneider, C.A., Rasband, W.S., and Eliceiri, K.W. (2012). NIH Image to ImageJ: 25 years of image analysis. Nat. Methods *9*, 671–675. https://doi.org/10.1038/nmeth.2089.

69. Fernández-Vizarra, E., Ferrín, G., Pérez-Martos, A., Fernández-Silva, P., Zeviani, M., and Enríquez, J.A. (2010). Isolation of mitochondria for biogenetical studies: An update. Mitochondrion *10*, 253–262. https://doi.org/10.1016/j.mito.2009.12.148.

70. Acín-Pérez, R., Fernández-Silva, P., Peleato, M.L., Pérez-Martos, A., and Enriquez, J.A. (2008). Respiratory active mitochondrial supercomplexes. Mol Cell *32*, 529–539. https://doi.org/10.1016/j.molcel.2008.10.021.

71. Matyash, V., Liebisch, G., Kurzchalia, T.V., Shevchenko, A., and Schwudke, D. (2008). Lipid extraction by methyl-*tert*-butyl ether for high-throughput lipidomics. J. Lipid Res. *49*, 1137–1146. https://doi.org/10.1194/jlr.d700041-jlr200.

72. Robinson, D.R.L., Hock, D.H., Muellner-Wong, L., Kugapreethan, R., Reljic, B., Surgenor, E.E., Rodrigues, C.H.M., Caruana, N.J., and Stroud, D.A. (2022). Applying Sodium Carbonate Extraction Mass Spectrometry to Investigate Defects in the Mitochondrial Respiratory Chain. Front. Cell Dev. Biol. *10*, 786268. https://doi.org/10.3389/fcell.2022.786268.

Please cite this article in press as: Liang et al., Formation of I_2+III_2 supercomplex rescues respiratory chain defects, Cell Metabolism (2024), https://doi.org/10.1016/j.cmet.2024.11.011

73. Cox, J., and Mann, M. (2008). MaxQuant enables high peptide identification rates, individualized p.p.b.-range mass accuracies and proteome-wide protein quantification. Nat. Biotechnol. *26*, 1367–1372. https://doi.org/10.1038/nbt.1511.

74. Tyanova, S., Temu, T., Sinitcyn, P., Carlson, A., Hein, M.Y., Geiger, T., Mann, M., and Cox, J. (2016). The Perseus computational platform for comprehensive analysis of (prote)omics data. Nat. Methods *13*, 731–740. https://doi.org/10.1038/nmeth.3901.

75. Calvo, S.E., Clauser, K.R., and Mootha, V.K. (2015). MitoCarta2.0: an updated inventory of mammalian mitochondrial proteins. Nucleic Acids Res. *44*, D1251–D1257. https://doi.org/10.1093/nar/gkv1003.

76. Giese, H., Meisterknecht, J., Heidler, J., and Wittig, I. (2020). Mitochondrial Gene Expression: Methods and Protocols. Methods Mol. Biol. *2192*, 269–285. https://doi.org/10.1007/978-1-0716-0834-0_19.

77. Shalem, O., Sanjana, N.E., Hartenian, E., Shi, X., Scott, D.A., Mikkelsen, T.S., Heckl, D., Ebert, B.L., Root, D.E., Doench, J.G., and Zhang, F. (2014). Genome-Scale CRISPR-Cas9 Knockout Screening in Human Cells. Science *343*, 84–87. https://doi.org/10.1126/science.1247005.

78. Maldonado, M., Padavannil, A., Zhou, L., Guo, F., and Letts, J.A. (2020). Atomic structure of a mitochondrial complex I intermediate from vascular plants. eLife *9*, e56664. https://doi.org/10.7554/elife.56664.

79. Zheng, S.Q., Palovcak, E., Armache, J.-P., Verba, K.A., Cheng, Y., and Agard, D.A. (2017). MotionCor2: anisotropic correction of beam-induced motion for improved cryo-electron microscopy. Nat. Methods *14*, 331–332. https://doi.org/10.1038/nmeth.4193.

80. Rohou, A., and Grigorieff, N. (2015). CTFFIND4: Fast and accurate defocus estimation from electron micrographs. J. Struct. Biol. *192*, 216–221. https://doi.org/10.1016/j.jsb.2015.08.008.

81. Zivanov, J., Nakane, T., Forsberg, B.O., Kimanius, D., Hagen, W.J., Lindahl, E., and Scheres, S.H.W. (2018). New tools for automated high-resolution cryo-EM structure determination in RELION-3. eLife *7*, e421661. https://doi.org/10.7554/elife.42166.

82. Wagner, T., Merino, F., Stabrin, M., Moriya, T., Antoni, C., Apelbaum, A., Hagel, P., Sitsel, O., Raisch, T., Prumbaum, D., et al. (2019). SPHIRE-crYOLO is a fast and accurate fully automated particle picker for cryo-EM. Commun. Biol. *2*, 218. https://doi.org/10.1038/s42003-019-0437-z.

83. Punjani, A., Zhang, H., and Fleet, D.J. (2020). Non-uniform refinement: adaptive regularization improves single-particle cryo-EM reconstruction. Nat. Methods *17*, 1214–1221. https://doi.org/10.1038/s41592-020-00990-8.

84. Liebschner, D., Afonine, P.V., Baker, M.L., Bunkóczi, G., Chen, V.B., Croll, T.I., Hintze, B., Hung, L.-W., Jain, S., McCoy, A.J., et al. (2019). Macromolecular structure determination using X-rays, neutrons and electrons: recent developments in *Phenix*. Acta Crystallogr. Sect. D *75*, 861–877. https://doi.org/10.1107/s2059798319011471.

85. Emsley, P., Lohkamp, B., Scott, W.G., and Cowtan, K. (2010). Features and development of *Coot*. Acta Crystallogr. Sect. D *66*, 486–501. https://doi.org/10.1107/s0907444910007493.

86. Spinazzi, M., Casarin, A., Pertegato, V., Salviati, L., and Angelini, C. (2012). Assessment of mitochondrial respiratory chain enzymatic activities on tissues and cultured cells. Nat Protoc. *7*, 1235–1246. https://doi.org/10.1038/nprot.2012.058.

87. Wong, H.-S., Monternier, P.-A., and Brand, M.D. (2019). S1QELs suppress mitochondrial superoxide/hydrogen peroxide production from site IQ without inhibiting reverse electron flow through Complex I. Free Radical Biol. Med. *143*, 545–559. https://doi.org/10.1016/j.freeradbiomed.2019.09.006.

88. National Research Council (2011). Guide for the Care and Use of Laboratory Animals, Eighth Edition (National Academy Press). https://doi.org/10.17226/12910.

89. Cai, Z.P., Shen, Z., Kaer, L.V., and Becker, L.C. (2008). Ischemic preconditioning-induced cardioprotection is lost in mice with immunoproteasome subunit low molecular mass polypeptide-2 deficiency. FASEB J. *22*, 4248–4257. https://doi.org/10.1096/fj.08-105940.

90. Zu, L., Bedja, D., Fox-Talbot, K., Gabrielson, K.L., Kaer, L.V., Becker, L.C., and Cai, Z.P. (2010). Evidence for a role of immunoproteasomes in regulating cardiac muscle mass in diabetic mice. J. Mol. Cell. Cardiol. *49*, 5–15. https://doi.org/10.1016/j.yjmcc.2010.02.007.

91. Glancy, B., Willis, W.T., Chess, D.J., and Balaban, R.S. (2013). Effect of Calcium on the Oxidative Phosphorylation Cascade in Skeletal Muscle Mitochondria. Biochemistry *52*, 2793–2809. https://doi.org/10.1021/bi3015983.

92. Messer, J.I., Jackman, M.R., and Willis, W.T. (2004). Pyruvate and citric acid cycle carbon requirements in isolated skeletal muscle mitochondria. Am. J. Physiol. Cell Physiol. *286*, C565–C572. https://doi.org/10.1152/ajpcell.00146.2003.

93. Golding, E.M., Teague, W.E., Jr., and Dobson, G.P. (1995). Adjustment of *K*′ to Varying pH and pMg for the Creatine Kinase, Adenylate Kinase and Atp Hydrolysis Equilibria Permitting Quantitative Bioenergetic Assessment. J. Exp. Biol. *198*, 1775–1782. https://doi.org/10.1242/jeb.198.8.1775.

94. Teague, W.E., Jr., Golding, E.M., and Dobson, G.P. (1996). Adjustment of *K*’ for the creatine kinase, adenylate kinase and ATP hydrolysis equilibria to varying temperature and ionic strength. J. Exp. Biol. *199*, 509–512. https://doi.org/10.1242/jeb.199.2.509.

95. Burger, N., Logan, A., Prime, T.A., Mottahedin, A., Caldwell, S.T., Krieg, T., Hartley, R.C., James, A.M., and Murphy, M.P. (2020). A sensitive mass spectrometric assay for mitochondrial CoQ pool redox state *in vivo*. Free Radic. Biol. Med. *147*, 37–47. https://doi.org/10.1016/j.freeradbiomed.2019.11.028.

96. Buján, N., Arias, A., Montero, R., García-Villoria, J., Lissens, W., Seneca, S., Espinós, C., Navas, P., De Meirleir, L., Artuch, R., et al. (2014). Characterization of CoQ_{10} biosynthesis in fibroblasts of patients with primary and secondary CoQ_{10} deficiency. J. Inherit. Metab. Dis. *37*, 53–62. https://doi.org/10.1007/s10545-013-9620-4.

97. Pandey, R., Riley, C.L., Mills, E.M., and Tiziani, S. (2018). Highly sensitive and selective determination of redox states of coenzymes Q_9 and Q_{10} in mice tissues: Application of orbitrap mass spectrometry. Anal. Chim. Acta *1011*, 68–76. https://doi.org/10.1016/j.aca.2018.01.066.

Please cite this article in press as: Liang et al., Formation of I_2+III_2 supercomplex rescues respiratory chain defects, Cell Metabolism (2024), https://doi.org/10.1016/j.cmet.2024.11.011

STAR★METHODS

KEY RESOURCES TABLE

REAGENT or RESOURCE	SOURCE	IDENTIFIER
Antibodies		
Rabbit polyclonal anti-BRAWNIN	This paper	RRID: AB_11005682
Mouse monoclonal anti-COX4I1	AB Clonal	Cat#A10098; RRID: AB_2757620
Rabbit monoclonal anti-GAPDH	Cell signaling Technology	Cat#2118; RRID: AB_561053
Mouse monoclonal anti-MTCO1	Abcam	Cat#Ab14705; RRID: AB_2084810
Mouse monoclonal anti-NDUFA9	Invitrogen	Cat#459100; RRID: AB_2532223
Rabbit polyclonal anti-NDUFB8	ProteinTech	Cat#11123-1-AP; RRID: AB_2150970
Rabbit polyclonal anti-SDHA	AB Clonal	Cat#A2594; RRID: AB_2764479
Rabbit polyclonal anti-TIM23	ProteinTech	Cat#11123-1-AP; RRID: AB_615045
Rabbit polyclonal anti-TOMM70	AB Clonal	Cat#A4349; RRID: AB_2765636
Rabbit polyclonal anti-UQCC1	Sigma-Aldrich	Cat#HPA034875; RRID: AB_10603226
Rabbit polyclonal anti-UQCRC1	AB Clonal	Cat#A3339; RRID: AB_2765058
Rabbit polyclonal anti-UQCRC2	AB Clonal	Cat#A4181; RRID: AB_2765543
Mouse monoclonal anti-UQCRFS1	Abcam	Cat#Ab14746; RRID: AB_301445
Chemicals, peptides, and recombinant proteins		
Sucrose	Sigma-Aldrich	Cat#S3089
Ethylenediaminetetraacetic acid, ACS reagent, 99.4-100.6%, powder	Sigma-Aldrich	Cat#E9884
Trizma® base, anhydrous, free-flowing, Redi-Dri™, ≥99.9%	Sigma-Aldrich	Cat#RDD008
n-Dodecyl β-D-maltoside, ≥98% (GC)	Sigma-Aldrich	Cat#D4641
Digitonin	Sigma-Aldrich	Cat#D141
D-Sorbitol, ≥98%	Sigma-Aldrich	Cat#S1876
Lipofectamine 3000	Invitrogen	Cat#L3000015
Hexadimethrine bromide, ≥94% (titration)	Sigma-Aldrich	Cat#H9268
Puromycin	Invivogen	Cat#ant-pr
G418	Invivogen	Cat#ant-gn
Blotting-Grade Blocker	Bio-Rad	Cat#1706404
20X Tris Buffered Saline (TBS) Buffer, Ultra Pure Grade	1st base	Cat#BUF-3030-20X4L
TWEEN® 20, viscous liquid	Sigma-Aldrich	Cat#P1379
NativePAGE™ Running Buffer (20X)	Invitrogen	Cat#BN2001
NativePAGE™ Cathode Buffer Additive (20X)	Invitrogen	Cat#BN2002
NativePAGE™ 5% G-250 Sample Additive	Invitrogen	Cat#BN2004
NativePAGE™ Sample Buffer (4X)	Invitrogen	Cat#BN2003
20X MES SDS Running Buffer	Invitrogen	Cat#B0002
cOmplete™, Mini Protease Inhibitor Cocktail	Roche	Cat#11836153001
cOmplete™, Mini, EDTA-free Protease Inhibitor Cocktail	Roche	Cat#11836170001
Methanol, for analysis EMSURE® ACS,ISO,Reag. Ph Eur	Merck	Cat#1.06009.2511
Acetic acid (glacial) 100%, anhydrous for analysis EMSURE® ACS,ISO,Reag. Ph Eur	Merck	Cat#1.00063.2500
Chloroform, >99.0%(GC)	Kanto Chemical	Cat#07278-00
Palmitic acid, [1-^{14}C]-, 50 µCi	Perkin Elmer	Cat#NEC075H050UC
DMEM/High glucose (4500mg/ml) with L-glutamine; without sodium pyruvate	HyClone	Cat#SH30022.01
DMEM/Low glucose (1000mg/ml) with L-glutamine, sodium pyruvate	HyClone	Cat#SH30021.01

(*Continued on next page*)

Continued

REAGENT or RESOURCE	SOURCE	IDENTIFIER
DMEM, high glucose, no glutamine, no methionine, no cystine	Gibco	Cat#21013024
Sodium pyruvate solution, 100 mM, sterile-filtered, BioReagent, suitable for cell culture	Sigma-Aldrich	Cat#S8636
Penicillin-Streptomycin (10,000 U/mL)	Gibco	Cat#15140-122
Fetal Bovine Serum, South American Origin, Heat Inactivated	HyClone	Cat#SV30160.03
Triton™ X-100, laboratory grade	Sigma-Aldrich	Cat#X100
Bovine Serum Albumin, heat shock fraction, protease free, fatty acid free, essentially globulin free, pH 7, ≥98%	Sigma-Aldrich	Cat#A7030
Sodium deoxycholate, ≥97% (titration)	Sigma-Aldrich	Cat#D6750
Sodium dodecyl sulfate, BioReagent, suitable for electrophoresis, for molecular biology, ≥98.5% (GC)	Sigma-Aldrich	Cat#L3771
Glycerol, ACS reagent, ≥99.5%	Sigma-Aldrich	Cat#G7893
HEPES, ≥99.5% (titration)	Sigma-Aldrich	Cat#H3375
Magnesium chloride, anhydrous, ≥98%	Sigma-Aldrich	Cat#M8266
Ambion™ RNase I, cloned, 100 U/μL	Invitrogen	Cat#AM2294
SUPERase•In™ RNase Inhibitor (20 U/μL)	Invitrogen	Cat#AM2694
L-Glutamine (200 mM)	Gibco	Cat#25030081
D-(+)-Glucose solution, 100 g/L in H2O, sterile-filtered, BioXtra, suitable for cell culture	Sigma-Aldrich	Cat#G8644
Oligomycin A, ≥99% (HPLC)	Sigma-Aldrich	Cat#75351
Carbonyl cyanide 4-(trifluoromethoxy)phenylhydrazone ≥98% (TLC), powder	Sigma-Aldrich	Cat#C2920
Rotenone, ≥95%	Sigma-Aldrich	Cat#R8875
Antimycin A from Streptomyces sp.	Sigma-Aldrich	Cat#A8674
5,5′-Dithiobis(2-nitrobenzoic acid), ≥98%, BioReagent, suitable for determination of sulfhydryl groups	Sigma-Aldrich	Cat#D8130
Acetyl coenzyme A, trilithium salt, trihydrate	MP Biomedicals	Cat#100490
Oxaloacetic acid, ≥97% (HPLC)	Sigma-Aldrich	Cat#O4126
Trypsin-EDTA (0.25%), phenol red	Gibco	Cat#25200-056
DPBS without calcium, magnesium	HyClone	Cat#SH30028.02
Sodium hydroxide, reagent grade, 97%, powder	Sigma-Aldrich	Cat#655104
Agarose	1st base	Cat#BIO-1000
2-Chloroacetamide, ≥98%	Sigma-Aldrich	Cat#C0267
Bond-Breaker™ TCEP Solution, Neutral pH	Thermo Fisher Scientific	Cat#77720
Pierce™ Trypsin Protease, MS Grade	Thermo Fisher Scientific	Cat#90057
Trifluoroacetic acid, eluent additive for LC-MS, LiChropur, ≥99.0% (GC)	Sigma-Aldrich	Cat#80457
Acetonitrile, anhydrous, 99.8%	Sigma-Aldrich	Cat#271004
Ammonium hydroxide solution, puriss., 30-33% NH3 in H2O	Sigma-Aldrich	Cat#05002
Pierce™ Formic Acid, LC-MS Grade	Thermo Fisher Scientific	Cat#TS-28905
Acetone, ACS reagent, ≥99.5%	Sigma-Aldrich	Cat#179124
Urea AR	Chem-Supply	Cat#UA001
Ammonium bicarbonate, BioUltra, ≥99.5% (T)	Sigma-Aldrich	Cat#09830
SYBRSafe	Sigma-Aldrich	Cat#S33102
TRIzol LS Reagent	ambion	Cat#10296028
Critical commercial assays		
Pierce BCA Protein Quantification Kit	Thermo	Cat#23225
iScript Reverse Transcription Supermix for RT-qPCR	Bio-Rad	Cat#1708841
iTaq Universal SYBR Green Supermix	Bio-Rad	Cat#1725124

(*Continued on next page*)

Please cite this article in press as: Liang et al., Formation of I_2+III_2 supercomplex rescues respiratory chain defects, Cell Metabolism (2024), https://doi.org/10.1016/j.cmet.2024.11.011

Continued

REAGENT or RESOURCE	SOURCE	IDENTIFIER
Experimental models: Cell lines		
Human HEK293T	ATCC	Cat#CRL-3216
Mouse C2C12	ATCC	Cat#CRL-1772
Experimental models: Organisms/strains		
Mouse: WT (C57BL/6J)	The Jackson Laboratory	Cat#000664
Mouse: $BR^{-/-}$ (C57BL/6J)	This paper	N/A
Oligonucleotides		
pLV-EF1-RFP	Gift from Navdeep Chandel Lab	N/A
pLV-EF1-AOX-RFP	Gift from Navdeep Chandel Lab	N/A
Source Data		
Data S1 – Source Data	Mendeley Data	N/A
Software and algorithms		
ImageJ	Schneider et al., 2012[68]	https://imagej.nih.gov/ij/
Image Lab Software for PC Version 6.1	Bio-Rad	SOFT-LIT-170-9690-ILSPC-V-6-1

METHOD DETAILS

Animals

The BR KO mice are on a C57BL/6J background and were generated as previously reported.[37] They were kept at a temperature range of 21-24°C with a relative humidity of 40–60%, with unrestricted access to water and chow diet. All animal procedures were authorized by the Duke-NUS, SingHealth Institutional Animal Care and Use Committee.

Indirect Calorimetry by Phenomaster

Whole-body metabolic parameters were assessed by open-circuit indirect calorimetry. Animals were singly housed in the PhenoMaster automated home-cage system (TSE Systems, Germany) in a temperature- and humidity-controlled environment with a 12 h light/dark cycle. Parameters including oxygen consumption (VO_2), carbon dioxide production (VCO_2), food intake and locomotor activity were measured simultaneously at 1 min time intervals. Energy expenditure was calculated from VO_2 and VCO_2. Locomotor activity was defined as the total number of infrared beam breaks in the X- and Y-axis. Mice were monitored for 6 consecutive overnight periods including an acclimatization period during the first light/dark cycle (day 0-1) which was not used for analysis. Animals were given *ad libitum* access to food and water except during fasting, when food access was restricted. To assess response to thermoneutrality and cold challenge, the climate chamber temperature was raised to 28°C and lowered to 4°C respectively. To access voluntary activity, home-cages were augmented with a rodent running disk. Voluntary running activity is approximated energy expenditure, which is elevated in the presence of the running wheels corrected for any baseline differences (i.e., with no running wheels).

Mouse treadmill exercise

WT and BR KO male littermates between 20-30 weeks were selected to perform treadmill exercise. Mice were habituated to a single-line enclosed metabolic treadmill equipped with a shock grid (Columbus Instruments) for 3 days prior to experiments. The exhaustive exercise test began with 10-min 0 m/min acclimation period followed by a speed of 6 m/min for 5 min, followed by increasing speed 3 m/min every 5 min. Once 20 m/min was reached, speed increased by 2 m/min every 2 min until exhaustion, defined as remaining on the shock grid for 10 seconds without engaging the treadmill despite repeated physical prompts to resume running. Total distance was calculated as the distance ran before exhaustion.

Cell lines

C2C12 (CRL-1772) were grown at 37 °C with 5% CO_2 unless otherwise specified. The cells were kept at sub-confluent densities in DMEM high glucose (4500 mg/ml) medium, supplemented with 10% FBS, 1 mM pyruvate, and 100 U/ml penicillin-streptomycin. HEK293T cells (CRL-3216) were also maintained in the same medium as C2C12 myoblasts. Both cell lines were procured from ATCC, and no additional verification was conducted. Cyt b mutant cybrids were a gift from Prof Anna Maria Ghelli from University of Bologna, and were maintained in DMEM high glucose (4500 mg/ml) medium, supplemented with 10% FBS, 1 mM pyruvate, 50 μg/ml uridine and 100 U/ml penicillin-streptomycin

Please cite this article in press as: Liang et al., Formation of I_2+III_2 supercomplex rescues respiratory chain defects, Cell Metabolism (2024), https://doi.org/10.1016/j.cmet.2024.11.011

Cell culture

Cell lines were maintained at sub-confluency. Cells were washed with PBS before being digested with 0.25% Trypsin-EDTA for 3 min at 37 °C. Trypsin was neutralized with equal volumes of complete DMEM media. Cell pellet was collected through centrifugation for 3 min at 300 × g. Desired number of cells were plated back with complete DMEM media or otherwise indicated.

Doxycycline Pulse Chase

C2C12 cells expressing either scr or BR gRNA1 were pulsed with 15 μg/ml doxycycline treatment for 8 days to minimize mitochondrial protein synthesis. To follow the accumulation of newly synthesized ETC complexes and their further association into SCs, samples were collected at different time points (0, 6, 15, 24, 48, 72, and 96 hours) after doxycycline removal. Whole-cell extracts and digitonin-solubilized mitochondrial particles were separated by SDS-PAGE or BN-PAGE, respectively, and analyzed by immunoblotting.

AAV production and infection

ORFs encoding the respective protein of interest with C-terminal FLAG-tag were cloned into psAAV-CMV construct. All constructs were delivered by AAV9 and the viruses were produced by Vector Core @ GIS (A*STAR, Singapore). To deliver the AAVs to target the cardiac muscle, we performed intrathoracic injection of P6 pups using a dose of 1 x 10^{10} vg per mouse. The pups were cryoanesthetized on ice prior to injection and allowed to recover under a heat lamp before being returned to the dam. Tissues were collected 6 weeks after neonatal AAV delivery.

Mitochondria isolation

Mitochondria were isolated from mouse tissues and cultured cells as described by Fernández-Vizarra, et al. and Acín-Pérez et al.,[69,70] respectively.

Briefly, mice were euthanized by CO_2 and desired tissues were immediately dissected after perfusions with PBS. Heart and skeletal muscles were minced carefully with a scissor and incubated in 10 volumes of heart mitochondria isolation buffer (75 mM sucrose, 225 mM sorbitol, 1mM EGTA, 0.1% fatty acid free BSA, 10 mM Tris-HCl, pH7.4) or skeletal muscle mitochondria isolation buffer (67 mM sucrose, 50 mM KCl, 10 mM EDTA, 0.1% fatty acid free BSA, 50 mM Tris-HCl, pH7.4) supplemented with 1x cOmplete protease inhibitors and 1 mM PMSF. Minced tissues were dounced in Potter-Elvehjem tissue grinders with PTFE pestles driven by a motorized drill for 10 to15 strokes. Efficiency of tissue homogenization was inspected by white field microscopy. Homogenates were transferred to tubes and spun at 600 × g for 10 min at 4 °C. The supernatant was collected and spun at 7000 × g for 15 min at 4°C. The mitochondrial pellet was gently resuspended in Buffer C (320 mM sucrose, 1mM EDTA, 10mM Tris-HCl, pH7.4). Mitochondrial protein content was measured by BCA assay. Desired quantity of mitochondria was aliquoted and pelleted at 7000 × g for 15 min at 4 °C. Mitochondrial pellets were used directly or stored at -80 °C for future biochemical analysis.

For isolating mitochondria from cultured cells, cell pellets were harvested, washed in PBS and then resuspended in Buffer A (83 mM sucrose, 10 mM HEPES pH7.4) supplemented with 1x cOmplete protease inhibitors and 1 mM PMSF, and incubated for 10 min on ice. Cells were then dounced in Potter-Elvehjem tissue grinders as described above. Homogenates were spun at 1,000 × g for 10 min at 4 °C. The supernatant was transferred to a new tube and remaining pellets were resuspended again in Buffer B (250 mM sucrose, 10 mM HEPES pH7.4) supplemented with 1x cOmplete protease inhibitors and 1mM PMSF. The extraction was repeated, and homogenates were spun at 1,000 × g for 10 min at 4 °C. The supernatant of both extractions was combined and spun at 12,000 × g for 15 min at 4 °C. The mitochondria pellet was resuspended in Buffer C supplemented with 1x cOmplete protease inhibitors and 1 mM PMSF with protein content quantified using a Pierce BCA kit.

Cardiolipin Quantification

Lipids were extracted from mitochondria using a modified Matyash lipid extraction.[71] Briefly, a mixture of cold methyl-tert-butyl ether, methanol, and internal standards (SPLASH Mix Avanti Polar Lipids 330707 and Cardiolipin Mix I Avanti Polar Lipids LM6003) was added to 150 μg of mitochondrial protein. The samples were vortexed and then sonicated for 1 min. The samples were then incubated on ice for 15 min and vortexed every 5 min. Phase separation was induced by adding 300 μL of H_2O and centrifuging at 15,000 × g, and the organic phase was then dried using a SpeedVac. The dried lipids were reconstituted in a 9:1 methanol:toluene mixture. Liquid chromatography-mass spectrometry (LC-MS) was then performed on the reconstituted lipids using an Agilent 6490 UPLC-QQQ mass spectrometer (PC species) and an Agilent 6530 UPLC-QTOF mass spectrometer (CL species).

C2C12 mitochondrial proteome analysis

C2C12 mitochondria were isolated as described above and processed using S-Trap columns as described before.[72] Peptides were reconstituted in 0.1% TFA, 2% acetonitrile (ACN) and analyzed via LC-MS/MS, carried out on an Orbitrap Eclipse Plus (Thermo Scientific) coupled with an Ultimate 3000 RSLC nanoHPLC (Dionex Ultimate 3000). The LC system was equipped with an Acclaim Pepmap nano-trap (Dionex-C18, 100 Å, 75 μm x 2 cm) and RSLC analytical column (Dionex-C18, 100 Å, 75 μm x 50 cm). Peptides were injected to the trap column at an isocratic flow of 5 μL/min of 2% (v/v) ACN containing 0.1% (v/v) formic acid for 5 min applied before the trap column was switched in-line with the analytical column. The in-house 125 minute gradient was formed from 5% DMSO in 0.1% (v/v) formic acid (solvent A) and 5% DMSO in 100% (v/v) ACN and 0.1% (v/v) formic acid (solvent B). The mass spectrometer was operated in positive-ionization mode with spray voltage set at 2.0 kV and source temperature at 275 °C in data-dependent

Please cite this article in press as: Liang et al., Formation of I_2+III_2 supercomplex rescues respiratory chain defects, Cell Metabolism (2024), https://doi.org/10.1016/j.cmet.2024.11.011

acquisition mode with MS spectra scanning from m/z 375-1500 at 120,000 resolution with AGC target of 4e5. The "top speed" acquisition method mode (3 sec cycle time) on the most intense precursor was used whereby peptide ions with charge states $\geq$2-7 were isolated with isolation window of 1.6 m/z and fragmented with high energy collision (HCD) mode with stepped collision energy of 30 ± 5% (Eclipse). Fragment ion spectra were acquired in the Orbitrap at 15,000 resolution. Dynamic exclusion was activated for 30s.

Raw files were analysed using MaxQuant platform[73] (version 2.0.1.0) and searched against UniProt mouse database (March 2021) using default LFQ search parameters. For this search Trypsin/P cleavage specificity (cleaves after lysine or arginine, even when proline is present) was used with a maximum of 2 missed cleavages. Oxidation of methionine and N-terminal acetylation were specified as variable modifications. Carbamidomethylation of cysteine was set as a fixed modification. A search tolerance of 4.5 ppm was used for MS1 and 20 ppm for MS2 matching. False discovery rates (FDR) were determined through the target-decoy approach set to 1% for both peptides and proteins. Data analysis was conducted using the Perseus framework[74] (version 1.6.13.0) as previously described.[37] Briefly, protein groups labelled "contaminants" and "reverse" were removed and LFQ intensity values grouped into experimental groups consisting of three replicates each. Protein identifications were filtered to remove those identified from <2 unique peptides and the presence of at least one group with 100% valid values. Annotations for proteins present in the Mitocarta2.0 dataset[75] were added through matching by gene name and rows filtered to include only mitochondrial entries. A two-sample t-test was conducted between each experimental group and its control, with results displayed as a volcano plot.

Complexome Profiling

Complexome profiling procedure is adapted from previous work.[76]

Stoichiometry Determination

Stoichiometry of the SC-XL was determined using IBAQ values data from each slice analysed in complexome profiling and illustrated in Table S1. Band 36 corresponds to the SC1 SC with the consensus stoichiometry of I+III_2, band 37 is the SC2 SC with consensus stoichiometry of I+III_2+IV. Band 37 from WT mitochondria was used as the reference complex to estimate the relative stoichiometry in band 40 corresponding to the SC-XL. A normalized average IBAQ value for each complex was first derived for each band by taking the mean of IBAQ values of all structural subunits (excluding assembly factors) of each complex, normalized to total input. The average IBAQ value for CI in each band was set to 1, and that of CIII and CIV was normalized to CI to get relative stoichiometry ratios. These values were further fitted to that of the SC1, which harbors CI:CIII:CIV in a 1:2:1 ratio, reflecting the fact that CIII exists as a dimer. The relative complex ratio of band 40 SC-XL from the KO was then inferred by comparison to this 1:2:1 ratio. This method predicts the SC1 from WT to be of the ratio I+$III_{1.72}$+$IV_{0.2,}$ which rounds up to I+III_2 with the assumption that the substoichiometric presence of CIV reflects background contamination of CIV in the SC region of the gel. Similarly, this method predicts that the SC-XL from WT has a CI:CIII:CIV ratio of 1:1.15:0.1.. Since CIII always exists as a dimer, this ratio should be multiplied by 2 to fit a CIII dimer to give a CI:CIII:CIV ratio of 2:2.30:0.2, which rounds up to a predicted stoichiometry of I_2+III_2 , once again with background contamination of CIV accounting for the substoichiometric presence of CIV.

SDS-PAGE and immunoblotting

Cell pellets, purified mitochondria, and mouse tissues were lysed in RIPA buffer (10mM Tris-HCl, pH8.0, 1% Triton X-100, 0.5% sodium deoxycholate, 0.1% SDS, 140mM NaCl) supplemented with 1x cOmplete protease inhibitors and 1mM PMSF. For tough mouse tissues like skeletal and heart, samples were lysed on a MagNA Lyser (Roche) by two 30 s cycles at 5000 rpm. Protein concentrations were determined by a BCA assay (Thermo). After protein concentration normalization, lysates were mixed with 4x protein loading buffer (0.2M Tris-HCl, pH6.5, 50 mM DTT, 8% SDS, 4.3M glycerol) and incubated at 95°C for 5 min in a thermomixer. Proteins were then resolved on 4-12% Bis-Tris precast gels using MES running buffer and transferred to PVDF membranes (Bio-Rad) using a Trans-Blot Turbo system (Bio-Rad). Membranes were blocked in milk TBST (5% skim milk powder dissolved in TBS with 0.1% Tween 20) for 1 h at room temperature and incubated with diluted primary antibodies in milk TBST at 4°C for overnight. Membranes were then extensively washed and incubated with appropriate HRP conjugated secondary antibodies at room temperature for 1 h in milk TBST and extensively washed again. ECLs were prepared following the user manual and evenly distributed to membranes. Chemiluminescence was recorded by a Chemidoc Touch imager. Quantifications were performed using Image Lab.

Native PAGE

For Blue Native PAGE (BN PAGE), mitochondrial proteins were solubilized in 1x Native PAGE Sample Buffer supplemented with 8 g of digitonin per g of mitochondrial protein and 1x cOmplete protease inhibitor for 20 min on ice. Lysate was cleared by spin at 20,000 × g for 10 min at 4°C and then supplemented with 0.5% G250 sample additive. Mixed solutions were loaded onto 3-12% Native PAGE Bis-Tris gels. Electrophoresis was performed at 150 V for 30 min in the presence of dark blue cathode running buffer and then at 250 V for 1 h with light blue cathode running buffer with ice bath. NativePAGE gels were then imaged with the Coomassie Blue mode on a Bio-Rad Chemidoc Touch imager before transferred to PVDF membranes (Bio-Rad) using a Trans-Blot Semi-Dry system (Bio-Rad). Membranes were then fixed with 8% acetic acid for 15 min before washing in water for 5 min. Membranes were destained in methanol until bands were barely visible and then blocked in 5% milk TBST for 1h at RT. Membranes were then processed as standard western blots.

For Clear Native PAGE (CN-PAGE), mitochondrial proteins were processed similarly as BN-PAGE. The solublized mitochondria were supplemented with 0.5% G250 sample additive before loading onto Native PAGE gels. Electrophoresis was performed at

Please cite this article in press as: Liang et al., Formation of I_2+III_2 supercomplex rescues respiratory chain defects, Cell Metabolism (2024), https://doi.org/10.1016/j.cmet.2024.11.011

150 V for 30 min in the presence of light blue cathode running buffer and then at 250 V for 150 min with clear cathode running buffer with ice bath. The gel was then incubated in CI substrate solution (2 mM Tris-HCl, pH 7.4, 0.1 mg/ml NADH, 2.5 mg/ml Nitrotetrazolium Blue chloride (NTB)). Appearance of violet bands is indicative of CI activity. The reaction was stopped with 10% acetic acid. Images were acquired using a scanner.

Respiratory activity of excised gel slices

WT mice were fasted overnight, and hearts were harvested for mitochondria isolation. Freshly isolated mitochondria were solubilized with 8 g/g digitonin, and 100 μg of solubilized mitochondrial membranes were separated in a "light blue" NATIVE PAGE (30 minutes in dark cathode buffer at 150 V, 1.25 hours in light cathode buffer at 250 V). Gels were removed from plates, rinsed with milli-Q water, photographed with a CCD camera to quantitate protein amount using the Coomassie dye, and kept on ice and covered to prevent dehydration. Bands representing the various SCs (From SC1 to one band above the SC-XL (SC-XL+1)) were excised using razor blades under a dissection microscope, with each slice no thicker than 1mm. Each band was further excised into 3 equal segments across the lane and each of the 3 pieces was inserted into one well of a XFe96 Spheroid Microplate, tucking it into the lower chamber but avoiding the posts. Wells were covered with 180 μl of prewarmed buffer (70 mM sucrose, 220 mM mannitol, 10 mM KH_2PO_4, 5 mM $MgCl_2$, 2 mM HEPES, 1 mM EGTA, 0.4% fatty acid free BSA, 20 μM cytochrome c). Injections were made as follows (final concentration in well): Port A – 5 mM NADH; Port B: 80 μM antimycin; Port C: 0.1 μM TMPD + Ascorbate; Port D: 10 mM KCN. Gel pieces with no protein were used as background controls. The background corrected OCR was normalized to protein amount quantitated by densitometry of the Coomasie staining.

Gene editing by CRISPR

gRNA cloning protocol is adapted from Shalem et al.[77] Oligos of gRNA sequences with appropriate links (CACCG added to forward oligo 5′ end; AAAC———C added to reverse oligo 5′ and 3′ ends) were obtained from IDT. gRNAs were then cloned into Lenti-CrisprV2-Puro plasmid using BsmBI digestion and T4 ligation as described in Shalem et al. gRNA sequences used for Crispr-Cas9 editing are included in Table S1. Sequence of constructs was validated by Sanger sequencing using a U6 promoter primer.

Virus production and transduction

4.4 million HEK293T cells were seeded in 10 cm dishes the day before transfection. On the day, 3 μg of respective lentiviral plasmids were transfected using Lipofectamine 3000 with other 3rd generation lentivirus production plasmids, namely pMDL, pREV, and pVSVG. The transfectants were left in culture for 6 hours before being exchanged with complete DMEM media. Crude virus was collected at 36 h and 60 h after the transfection. Vivaspin 100,000 MWCO columns (Sartorius) were used to purify and concentrate crude viruses.

25,000 C2C12 cells were seeded in 12 well plates the day before transduction. Appropriate amounts of virus were mixed with 8 μg/ml of hexadimethrine bromide (polybrene) before being added to respective wells for transduction. Cells were subcultured 3 days after transduction and selected with puromycin (1 μg/mL) or G418 (500 μg/mL).

Seahorse assay

15,000 C2C12 cells or 10,000 C2C12 cells were plated on Seahorse XF96 Cell Culture Microplates (Agilent) 1 day or 2 days before the MitoStress test, respectively. XFe96 sensor cartridge (Agilent) was hydrated with distilled water at 37 °C with no CO_2 the day prior to the MitoStress test. Drug treatment was performed 1 day before the assay. On the day of assay, cells were washed once and media were replaced with XF basal DMEM supplemented with 1 mM pyruvate, 2 mM glutamine, and 10 mM glucose OR 10 mM galactose. Pre-hydrated sensor cartridge was calibrated with Seahorse XF Calibrant (Agilent). Both cell culture plate and sensor cartridge were incubated at 37 °C with no CO_2 for at least 45 min before the assay. For MitoStress assay, 2 μM of oligomycin, 1 μM of FCCP, and 1μM of rotenone/antimycin were injected according to Seahorse MitoStress Assay Protocol (Agilent). Citrate synthase activity was performed for cell number normalization.

Isolated Mitochondria Seahorse and Electron Flow

20 μg of freshly isolated mitochondria from WT and BR KO heart were plated on Seahorse XF96 Cell Culture Microplates (Agilent). The plates were spun down at 2000 × g for 20 mins to ensure attachment of mitochondria to the plate. The reaction buffer consists of 70 mM sucrose, 220 mM mannitol, 10 mM KH_2PO_4, 5 mM $MgCl_2$, 2 mM HEPES, 1 mM EGTA and 0.4% fatty acid free BSA. Pre-hydrated sensor cartridge was calibrated with Seahorse XF Calibrant (Agilent). Both mitochondria culture plate and sensor cartridge were incubated at 37 °C with no CO_2 for at least 45 min before the assay. 10 mM sodium pyruvate and 5 mM sodium malate were supplemented for electron flow assay and isolated mitochondria seahorse assay with pyruvate/malate as fuel. 10 mM sodium succinate and 2 μM rotenone were supplemented for isolated mitochondria seahorse assay with succinate as fuel. 40 μM palmitoyl-L-carnitine was supplemented for isolated mitochondria seahorse assay with palmitate as fuel. For electron flow assay, 2 μM of rotenone, 4 mM of sodium succinate, 4 μM of antimycin A and 0.1 mM TMPD were injected according to Seahorse MitoStress Assay Protocol (Agilent). For isolated mitochondria seahorse assay, 3 mM of ADP, 3 μM of oligomycin, 4 μM of FCCP and 4 μM of antimycin A were injected according to Seahorse MitoStress Assay Protocol (Agilent). Citrate synthase activity was performed for cell number normalization.

Please cite this article in press as: Liang et al., Formation of I_2+III_2 supercomplex rescues respiratory chain defects, Cell Metabolism (2024), https://doi.org/10.1016/j.cmet.2024.11.011

Citrate synthase activity assay

Citrate synthase activity was performed on Seahorse XF96 Cell Culture Microplate (Agilent) right after seahorse assay or on plates frozen at -80 °C with the leftover medium aspirated. 113 μl of CS buffer (200 mM Tris buffer at pH8.0, 0.2% Triton X-100 (v/v), 100 μM DTNB in 100 mM Tris buffer at pH 8.0, 1 mM Acetyl-CoA) was added to wells. 5 μl of 10 mM oxaloacetic acid was added as the reaction substrate. Absorbance at 412 nM at 37 °C was recorded with a Tecan Microplate Reader M200 (Tecan) at a minimal time interval for 5 min.

Citrate Synthase activity was then calculated using the formula below:

$$\text{CS activity} = \sum_{i=1}^{n} \frac{\left(\left[\frac{A_i - A_0}{t_i - t_0}\right]\right)}{n} \quad (n \in N^*)$$

Where, n is the total number of absorbance records; A is the absorbance recorded; t is the time.

Electron transport chain complex purification

The following operations were carried out at 4℃ unless otherwise indicated. The mitochondria pellet was resuspended and lysed in milli-Q water at 10 mL/g (of starting mitochondria, wet weight) using a Dounce homogenizer, to which KCl was added to a final concentration of 150 mM. The mitochondrial membrane was pelleted by centrifugation at 32,000 x g for 45 minutes and washed once in buffer M10 (20 mM Tris pH 7.4, 50 mM NaCl, 1 mM EDTA, 2 mM dithiothreitol (DTT), 0.002% PMSF (w/v), 10% glycerol (v/v)) at 18 mL/g (of starting mitochondria). The resulting membrane pellet was resuspended in buffer M10 at 3 mL/g (of starting mitochondria) and the protein concentration was determined using a BCA assay (Pierce Thermo Fisher). The resuspended membranes were stored at 10 mg/mL of total protein at -80℃ in a final glycerol concentration of 30% (v/v) after dilution with buffer M90 (20 mM Tris pH 7.4, 50 mM NaCl, 1 mM EDTA, 2 mM DTT, 0.002% PMSF (w/v), 90% glycerol (v/v)). Usual yield was ~30 mg total membrane protein per gram of *M. musculus* heart tissue.

The thawed mitochondrial membrane resuspension was solubilized in buffer MX (30 mM HEPES pH 7.7, 150 mM potassium acetate, 0.002% PMSF, 10% (v/v) glycerol, 1 mM EDTA) by slow tumbling for 1 hour at 4℃ with 1% digitonin (w/v) at a detergent-to-protein ratio of 4:1 (w/w). The insoluble material was cleared by centrifugation at 16,000 x g for 20 minutes. The supernatant was concentrated in 100 kDa MWCO centrifugal concentrators to 0.250 mL and loaded on to a continuous 20% to 45% (w/v) sucrose gradient in SGB buffer (15 mM HEPES pH 7.8, 20 mM KCl, 0.01% GDN). After centrifugation in a SW40Ti swinging-bucket rotor at 149,176 x g for 23 hours, the sucrose gradients were fractionated using a Biocomp gradient profiler. Fractions were assayed for CI activity by running them on a 3%-12% Tris-glycine BN-PAGE gel and a nitrotetrazoleum blue in-gel assay was performed as previously described[78] (Figure S3E).Fractions displaying CI activity were pooled and concentrated to a final concentration of 5 mg/mL in exchange buffer (30 mM HEPES pH 7.7, 150 mM potassium acetate, 0.002% PMSF, 10% (v/v) glycerol, 1 mM EDTA, 0.005% GDN, 0.05% digitonin).

CryoEM grid preparation and data collection

Four microliters of concentrated sample from the sucrose gradients were applied onto a Quantifoil R1.2/1.3 300 mesh copper grids glow-discharged at 30 mA for 30 seconds before sample application. In a GP2, the grid was first incubated for 20 seconds at 95% humidity, then blotted for 4 seconds before plunge-freezing into liquid ethane cooled by liquid nitrogen. A total of 27167 movies (combined from three data sets) were collected using SerialEM on a 200 kV ThermoFisher Glacios microscope equipped with a Gatan Quantum K3 detector, at a nominal magnification of 56,818 (0.44 Å/pixel under super-resolution mode). A dose of 20 electrons/$Å^2$/s with 3-second exposure time was fractionated into 75 frames for each movie.

CryoEM image processing

The raw movies were binned 2-fold and motion-corrected using the MotionCor2,[79] followed by per-micrograph contrast transfer function (ctf) estimation using the CTFFIND 4.1,[80] both implemented in Relion 4.0.[81] Micrographs were then curated to remove images lacking high resolution ctf correlations. Particles were picked from the curated set of micrographs using TOPAZ.[82] The initial 1,165,315 picked particles from TOPAZ were extracted in Relion 4.0 with 672 $pixel^2$ boxes, followed by 2D classification, 3D *ab initio* reconstruction and 3D refinement in cryoSPARC v4.3.0. Iterative 2D classification and 3D *ab initio* reconstruction resulted in 382,876 good particles corresponding predominantly to SC-XL. SC I+III_2 and SC I+III_2+IV were also present in the set (Figure S4C). Homogenous refinement followed by non-uniform refinement[83] of the above set in cryoSPARC resulted in an initial reference map of 4.95 Å. Heterogeneous refinement of the particles (382,876 particles) into two classes using SC-XL, and SC I+III_2+IV volumes as starting models, classified the particles into two classes SC-XL (248,297 particles) and SC I+III_2+IV (134,579 particles). Homogenous refinement followed by non-uniform refinement[83] of the SC-XL set in cryoSPARC with per-particle defocus, scale and CTF refinement resulted in a reference map of 4.32 Å. 3D classification of the SC I+III_2+IV (134,579) set into two classes with SC I+III_2, and SC I+III_2+IV volumes resulted in 69,554 particles of SC I+III_2 and 65,035 particles of the SC I+III_2+IV. 3D classification of the scaled SC-XL set (248,297 particles) into four classes resulted in three classes that refined below 5 Å and one class that refined to ~8 Å, due to the per-particle scaling this classification likely separated particles based on micrograph quality, i.e., ice thickness, and thus, the particles in the low-resolution class were discarded. The three high-resolution SC-XL classes (182,132 particles) were combined and

Please cite this article in press as: Liang et al., Formation of I_2+III_2 supercomplex rescues respiratory chain defects, Cell Metabolism (2024), https://doi.org/10.1016/j.cmet.2024.11.011

refined using homogeneous and non-uniform refinement. This resulted in a final SC-XL map of 4.25 Å overall resolution. Focused local refinement of the above map in cryoSPARC using a $CIII_2$ mask, separate membrane arm (MA) masks for each of the CI protomers and separate peripheral arm (PA) masks for each of the CI protomers resulted in higher resolution maps for CIII (3.67 Å), MA (3.76 Å /3.82 Å) and PA (3.72 Å/3.82 Å) regions of the SC-XL map. A composite map was generated in Phenix-1.20.1[84] using the individual high-resolution focused maps. The composite map was used for model building and refinement.

Model building and refinement

All manual model building was performed in Coot 0.9.8.3[85] and refinements were performed in Phenix-1.20.1.[84] High resolution models of murine CI (2.39 Å PDB:8OM1)[44] and $CIII_2$ (2.60 Å PDB:7O3H)[3] were docked into the SC-XL composite map. The model-map fit was manually inspected, and the model was rebuilt where necessary to generate an initial SC-XL model. Secondary structure restraints were first automatically generated from the manually built model, then edited according to the outcome of the Phenix refinement. Bond length and angle restraints for metal ion coordination and amino acid side chain linkage were generated manually, and a ligand.cif file was also provided for non-default ligands in Phenix. The refined model was manually inspected and edited in Coot before the next round of Phenix refinement, and this iterative cycle continued until the model statistics converged before submission of maps and models to the EMDB and PDB databases. Model building and refinement statistics are provided in Table S1.

Sucrose gradient fractionation

Isolated mitochondria from mouse heart were solubilized with 8 g of digitonin per g of protein in 1x NativePAGE sample buffer with 1x cOmplete protease inhibitor. Lysates were spun down at 20,000 × g for 10 min before layered over a 5 to 60% linear sucrose gradient in sucrose buffer D (25 mM Tris-HCl pH7.4, 60 mM KCl) with 0.1% digitonin (w/v). Gradients were spun at 38,400 rpm for 18 h using a SW41Ti rotor in a Beckman Coulter Optima L-100XP ultracentrifuge. After centrifugation, gradients were fractionated manually at 700 μl per fraction to 17 fractions. Proteins from each fraction were extracted using methanol/chloroform and loaded onto a 4-12% Bis-Tris gel for SDS-PAGE.

Respiratory complex activity

The procedure was adapted from Spinazzi et al.[86] Briefly, isolated cardiac mitochondria or cellular mitochondria were used to perform this assay. Designated substrate and electron acceptors were added for colorimetric change detection. All measurements were taken using Tecan Microplate Reader M200 (Tecan) at 37 ℃ at a minimal time interval for 20 mins. Slope of the absorbance measurements against time was regarded as the activity of respective respiratory complexes.

Site Specific Respiratory ROS quantification

The protocol was adapted from Wong et al.[87] Both isolated mitochondria or plated cells with 0.0025% digitonin could be the assay materials. Briefly, the assay materials were incubated with 120mM KCl, 5 mM HEPES, 1 mM EGTA, 12.5 U/mL SOD1, 2.5 U/mL HRP, 12.5 μM Amplex UltraRed, 0.3% w/v FA free BSA. Respective substrates and inhibitors were added to catalyse the superoxide formation at designated ROS sites. For CI Q_R site, 5 mM sodium succinate and 0.3 μM S3QEL were used to induce CI Q_R ROS. 1 μM of nigericin was used to inhibit formation of CI Q_R ROS. For CIII Q_O site, 5 mM sodium succinate, 2.5 μM antimycin and 4 μM rotenone were used to induce CIII Q_O ROS. 2 μM of myxothiazol was used to inhibit the CIII Q_O ROS. Fluorescence readings over 540 nm/590 nm were documented and the slope against time was regarded as the ROS generation rate after subtracting the rate in the presence of the respective inhibitor. All results were normalized to the mitochondria amount quantified by CS assay.

To measure ROS produced at different energy depending state (Figure 5B), we combined the phosphocreatine clamp system from the Muoio lab (see above) with our Amplex UltraRed protocol for isolated mitochondria, using Buffer D (Potassium-MES (105 mM; pH = 7.2), KCl (30 mM), KH_2PO_4 (10 mM), $MgCl_2$ (5 mM), EGTA (1 m M), BSA (2.5 g/L)), supplemented with creatine (Cr; 5 mM), phosphocreatine (PCr; 1 mM), creatine kinase (CK; 20 U/mL), 5 mM sodium succinate, 2.5 μM antimycin, 4 μM rotenone, ATP (5mM), 12.5 U/mL SOD1, 12.5 μM Amplex UltraRed. Isolated mitochondria (0.025 mg/mL) was added to the assay buffer. PCr was added at concentrations of 3, 6, 9, 12, and 15 mM to gradually decrease respiration towards baseline levels. 2.5 U/mL HRP was added to start the reaction. A standard curve of Amplex UltraRed fluorescence using 0, 20, 40, 60, and 100 pmol of H_2O_2 in Buffer D (no supplementation) was obtained to quantitatively determine the levels of ROS produced at different respiratory stages. Fluorescence readings over 540 nm/590 nm were documented and the slope against time was regarded as the ROS generation rate after subtracting the rate in the presence of the respective inhibitor. All results were normalized to the mitochondria amount quantified by CS assay.

^{14}C 1-Palmitic acid coupled fatty acid oxidation assay (FAO)

The protocol was adapted from previous research.[66] Tissue homogenates or cell lysate with 0.0025% digitonin were used for FAO assay. The homogenates were incubated with oxidation reaction buffer (100 mM sucrose, 10 mM Tris-HCl pH 8, KH_2PO_4 5 mM, EDTA 0.2 mM, KCl 80 mM, $MgCl_2$ 1 mM, L-Carnitine 2 mM, malate 0.1 mM, Coenzyme A 0.05 mM, 2 mM ATP, and 1 mM DTT) with 0.7% BSA conjugated with 0.5 mM Palmitate. Experimental groups were supplemented with 10 μCi/mL of ^{14}C1-Palmitic acid. The reaction was conducted at 37 ℃ for 30 mins for tissue homogenates and 4 hours for cell lysates. The ^{14}C labelled CO_2 was extracted by perchloric acid and collected by NaOH infused filter paper disc in an Eppendorf tube for 1 hour. Paper discs were

Please cite this article in press as: Liang et al., Formation of I_2+III_2 supercomplex rescues respiratory chain defects, Cell Metabolism (2024), https://doi.org/10.1016/j.cmet.2024.11.011

then sent for scintillation and remaining solutions were centrifuged for 10 mins at 14000 × g before the supernatant was send for scintillation as well. Scintillation values were recorded using Tricarb machine (Perkin Elmer).

Ischemic Reperfusion Injury mouse model

The study utilized C57BL/6J wildtype and knockout (KO) mice, aged 8-12 weeks, to investigate the effects of 45-minute ischemia and 4-week reperfusion (IR) on cardiac function and structure. Sham animals were used as controls. Echocardiography was performed at 24 hours and 28 days of reperfusion to evaluate cardiac function, after which mice were euthanized and their hearts were collected. Cardiac sections were stained with Masson's trichrome to measure myocardial infarct size and fibrosis.

The experimental mice were obtained from Duke-NUS Medical School and housed in groups of four to five per cage in a room maintained at 23 ± 1 °C and 55 ± 5% humidity with a 12-hour light/dark cycle and had *ad libitum* access to food and water. All procedures performed in this study were approved by the Institutional Animal Care and Use Committee and adhered to the Guide for the Care and Use of Laboratory Animals published by the U.S. National Institutes of Health.[88]

Preparation of myocardial ischemia-reperfusion in mice: Prior to the procedure, mice were anesthetized with 3% isoflurane and intubated following established protocols.[89] A mouse ventilator was used to support respiration, while body temperature was maintained at 37 °C using a temperature control system throughout the experiment. Anesthesia was sustained with 2% isoflurane. An incision was made at the left 3-4 inter-rib space, and ischemia was induced by occluding the left coronary artery approximately 2 mm below the left auricle using a 7-0 surgical suture. Reperfusion was achieved by loosening the ligature. The chest was subsequently closed in two layers. Following the procedure, mice were returned to their cages and administered the pain reliever buprenorphine at a dosage of 0.1 mg/kg subcutaneously.

Echocardiography: *In vivo* assessment of cardiac function was performed on conscious mice using transthoracic echocardiography (GE Logiq e NextGen, 22MHz transducer; GE), employing methods described previously.[90] M-mode echocardiography was acquired from the left ventricle short axis view to measure interventricular septal thickness at end diastole (IVSd), left ventricular posterior wall thickness at end systole (LVPTs), left ventricular end diastolic diameter (LVEDD), and left ventricular end systolic diameter (LVESD). Fractional shortening (FS) and ejection fraction (EF) were calculated based on LVEDD and LVESD values [FS = (LVEDD - LVESD) / LVEDD%, EF = $(\mathrm{LVEDD}^2 - \mathrm{LVESD}^2) / \mathrm{LVEDD}^2\%$]. Three to five beats were averaged for each mouse study, and the analysis was performed by investigators blinded to the experimental conditions.

Assessment of myocardial infarct size: The measurement of myocardial infarct size followed established protocols.[89] Computerized planimetry using Image J software (NIH, Bethesda, MD, USA) was employed to determine the perimeter of cardiac sections and the length of the infarcted left ventricular (LV) wall. Myocardial infarct size was calculated as a percentage of the infarct length relative to the perimeter of the left ventricle.

Measurement of cardiac fibrosis: Hearts were fixed in 10% buffered formalin, embedded in paraffin, and sectioned at 5 μm, as described previously.[89] One middle section per heart was stained with Masson's trichrome. Fibrotic blue area and the total area were measured using computerized planimetry with Image J software (NIH). The fibrotic area was expressed as a percentage of the fibrotic area to the whole area. Three random fields per heart were counted and averaged, with a total of approximately 30 fields measured per group. The observer analyzing the cardiac sections was blinded to their origin.

Statistical analysis: Data are presented as mean ± standard error of the mean. Differences among groups were analyzed using Student's t-test. Statistical significance was considered if $p < 0.05$.

Mitochondrial Respirometric Phenotyping

The high-resolution measurement of O_2 consumption was conducted using the Oroboros Oxygraph-2K system (Oroboros Instruments). All experiments were carried out at a temperature of 37 °C and utilized a reaction volume of 2 mL. Within individual experiments, steady-state oxygen consumption rates (JO_2) were sequentially determined, ranging from near state 4 (non-phosphorylating state) to 95% of maximal state 3. This was achieved by employing a modified version of the creatine energetic clamp technique, as previously described by Glancy et al. and Messer et al.[91,92] In this assay, the free energy of ATP hydrolysis ($\Delta G'_{ATP}$) can be calculated based on known quantities of creatine (Cr), phosphocreatine (PCr), and ATP, combined with excess amounts of creatine kinase (CK) and the equilibrium constant for the CK reaction (i.e.,K_{CK}). Calculation of $\Delta G'_{ATP}$ was performed according to the following formula:

$$\Delta G'_{ATP} = \Delta G'^{\circ}_{ATP} + RT\ ln \frac{[Cr][P_i]}{[PCr][K'_{CK}]}$$

$\Delta G'^{\circ}_{ATP}$ represents the standard apparent transformed Gibbs energy (under a specified pH, ionic strength, free magnesium and pressure), R denotes the gas constant (8.3145 J K^{-1} mol^{-1}) and T is temperature in Kelvin (310.15 K). In this study, since the experiments involved sequential additions of phosphocreatine, both the $\Delta G'^{\circ}_{ATP}$ and K'_{CK} were determined at each titration step, taking into account changes in buffer ionic strength and free magnesium concentration, as previously described.[93,94] Calculation of $\Delta G'_{ATP}$ at each titration point was performed using a recently developed online tool (https://dmpio.github.io/bioenergetic-calculators/).

The assay buffer for all assays was Buffer D (Potassium-MES (105 mM; pH = 7.2), KCl (30 mM), KH_2PO_4 (10 mM), $MgCl_2$ (5 mM), EGTA (1 m M), BSA (2.5 g/L)), supplemented creatine (Cr; 5 mM), phosphocreatine (PCr; 1 mM) and creatine kinase (CK; 20 U/mL).

Please cite this article in press as: Liang et al., Formation of I_2+III_2 supercomplex rescues respiratory chain defects, Cell Metabolism (2024), https://doi.org/10.1016/j.cmet.2024.11.011

The experimental procedure involved the addition of isolated mitochondria (0.025 mg/mL) to the assay buffer, followed by the sequential addition of respiratory substrates and ATP (5 mM). Various substrate conditions were tested, including Octanoyl-carnitine/Malate (Oct/M; 0.2/2.5 mM), Glutamate/Malate (G/M; 10/2.5 mM), Pyruvate/Malate (Pyr/M; 5/2.5 mM), and Succinate/Rotenone (Succ/R; 10/0.005 mM). After the addition of substrates, PCr was sequentially added at concentrations of 3, 6, 9, 12, and 15 mM to gradually decrease JO_2 towards baseline levels. In experiments aimed at determining the ETC state 4 rate, ATP was omitted from the initial buffer and added after the addition of respiratory substrates. Plotting the calculated $\Delta G'_{ATP}$ against the corresponding JO_2 yields a linear relationship known as the force-flow relationship. The slope of this relationship represents the conductance/elasticity of the entire respiratory system under the specified substrate constraints.

Quantitative PCR Assay

Total RNA was extracted from respective cell lines using TRIzol. cDNA was obtained using iScript Reverse Transcription Kit. Quantitative measurement of cDNA amount was done using iTaq SYBR Green Kit and CFX384 Touch Real-Time PCR Detection System. All primers used were included in the Table S1.

mtDNA quantification

DNA from mouse gastrocnemius muscle was isolated using the Qiagen DNesay Blood and Tissue Kit (cat. No. 69504) according to the manufacturer's instructions. Quantitative measurement of mitochondrial (mtDNA) and nuclear DNA (nDNA) expression was performed using the BioRad iTaq Universal SYBR Green Supermix (Cat. No. 1725125) and the BioRad CFX384 Touch Real-Time PCR Detection System with the respective primers listed below. mtDNA gene expression was normalised to nDNA gene expression.

CoQ Measurement

The methods for the extraction CoQ were based on a previously reported method with slight modifications.[95,96] To extract CoQ from myoblast in 100 mm dishes, cells were washed twice with PBS, and pellets were re-suspended in 2 mL of lysis buffer (0.25 mM Sucrose, 2 mM EDTA, 10 mM Tris, and 100 UI/mL heparin, pH 7.4.), and sonicated twice for 5 seconds. These homogenates were also used to citrate synthase and protein quantification. To measure CoQ, nine hundred microliters of ethanol containing internal standard CoQ_{10}-d9 (IsoSciences, Ambler, PA) and 20 μM *tert*-butyl hydroquinone (TBHQ) (FUJIFILM Wako, Osaka, Japan) was added to 100 μL of homogenates. TBHQ was added to prevent oxidation of reduced CoQ. The cell suspensions were vortexed and centrifuged at 15,700 ×*g* for 10 min (4°C).

To extract CoQ from heart tissues, about 100 mg frozen tissue was weighed into cooled lysis tubes (Precellys, MK28-R) on dry ice. Then a mixture of 500 μl ice-cold acidified methanol and 500 μl hexane was added, and tissue was homogenized in the FastPrep-24 bead beating instrument (MP Biomedicals) three times for 30s at 6.0m/s (MK28 (2.8 mm) beads). The homogenate was transferred to fresh 1.5 ml tubes. In all cases the upper, CoQ-containing hexane layer was separated by centrifugation (5 min, 17,000×g, 4°C) and then dried down in 1 ml glass mass spectrometry vials. Dried samples were then resuspended in methanol containing 2 mM ammonium formate and diluted.

Reduced CoQ_9 and CoQ_{10} were required for use in the calibration curve measurement. However, since reduced CoQ is easily oxidized, reduced CoQ was prepared just before the analysis by reducing oxidized CoQ following a previously reported method with slight modification.[97] Briefly, 50 μL of CoQ was diluted in 1.95 ml hexane in a glass tube. Twenty milligrams of $NaBH_4$ were added and followed by the addition of 100 μL methanol, vortexed for 3 min, then placed in the dark for 5 min at room temperature. After reduction, 1 ml of water containing 100 μM EDTA was added to stop the reaction, vortexed for 1 min, and centrifuged 1,500 ×*g* for 5 min at 4°C. The upper layer containing reduced CoQ was transferred to a glass tube.

The method for measuring reduced and oxidized CoQ was based on the previously reported method with slight modifications.[102] An LC-MS/MS analysis was performed on an LC-electrospray ionization-MS (LC-ESI-MS) with triple quadrupole (Nexera X2 and LCMS-8060, Shimadzu, Kyoto, Japan). A Kinetex C18 column (100 mm x 2.1 mm, 2.6 μm, Phenomenex) and a guard column filled with the same packing material were used. The column temperature was kept at 40°C. The mobile phase was isocratic with 2 mM ammonium formate in methanol. The flow rate was 0.8 mL/min, the injection volume was 1-2 μL, and the run time was 6 min. The interface temperature was 300°C, the desolvation line temperature was 250°C, and the heat block temperature was 400°C. The nebulizing gas flow was 3 L/min, the heating gas flow was 10 L/min, and the drying gas flow was 10 L/min. The samples were kept at 4°C before injection by the autosampler. The MS/MS conditions for each target were optimized using the automated multiple reaction monitoring (MRM) optimization procedures in LabSolutions (Shimadzu). The MRM used for quantification was *m/z* 812.6 > 197.3 for oxidized CoQ_9, 814.6 > 197.2 for reduced CoQ_9, 880.5 > 197.1 for oxidized CoQ_{10}, 882.4 > 197.0 for reduced CoQ_{10}, and 890.4 > 206.2 for CoQ_{10}-d9 (internal standard). Standards and samples were quantified using the LabSolutions software program to determine the peak area for oxidized CoQ_9, reduced CoQ_9, oxidized CoQ_{10}, reduced CoQ_{10}, CoQ_{10}-d9, and the standard curves were used to determine the total amount of CoQ present in the samples.

Mouse Body Composition Measurement

Total fat and lean mass of mice was determined with EchoMRI using the 4 in 1 Composition Analyzer for live small animals (Echo Medical Systems) according to the manufacturer's instructions.

Please cite this article in press as: Liang et al., Formation of I_2+III_2 supercomplex rescues respiratory chain defects, Cell Metabolism (2024), https://doi.org/10.1016/j.cmet.2024.11.011

Statistical Analysis

Immunoblots were quantified using the volume tool of Image Lab (Version 6.0.1) with default background subtraction setting. Two-tailed unpaired t test was performed as indicted in the figure legend of specific experiments. p value < 0.05 is used as the cut off of significant different in this study. Actual levels of significance were marked in figure panels. No data point was excluded for data analysis.